Precession of spheroids under Lorentz violation and observational consequences for neutron stars

Rui Xu[1,*] Yong Gao[2,1] and Lijing Shao[1,3,†]

[1]*Kavli Institute for Astronomy and Astrophysics, Peking University, Beijing 100871, China*
[2]*Department of Astronomy, School of Physics, Peking University, Beijing 100871, China*
[3]*National Astronomical Observatories, Chinese Academy of Sciences, Beijing 100012, China*

The Standard-Model Extension (SME) is an effective-field-theoretic framework that catalogs all Lorentz-violating field operators. The anisotropic correction from the minimal gravitational SME to Newtonian gravitational energy for spheroids is studied, and the rotation of rigid spheroids is solved with the perturbation method and numerical approach. The well-known forced precession solution given by Nordtvedt in the parametrized post-Newtonian formalism is recovered and applied to two observed solitary millisecond pulsars to set bounds on the coefficients for Lorentz violation in the SME framework. A different solution, which describes the rotation of an otherwise free-precessing star in the presence of Lorentz violation, is found, and its consequences on pulsar signals and continuous gravitational waves emitted by neutron stars (NSs) are investigated. The study provides new possible tests of Lorentz violation once free-precessing NSs are firmly identified in the future.

I. INTRODUCTION

Lorentz invariance, which claims the equivalence between any two inertial reference frames in formulating the laws of physics, is a fundamental principle in both general relativity (GR) and the Standard Model of particle physics. However, in pursuing a unified theory of gravity and quantum particles, violation of Lorentz invariance was suggested [1–5] and has been treated as a possible suppressed effect emerging from the Planck scale where the unified theory lives. Therefore, searching for Lorentz-invariance violation in high-precision terrestrial experiments and astrophysical observations [5–7] not only serves as a necessary test of our current best knowledge of the laws of physics, but also provides us the chance to obtain information on the underlying theory of quantum gravity that is otherwise unattainable directly in the experiments and observations with limited energy scales.

A practical framework to study Lorentz violation without digging into the extensive intricacies of the underlying theory is the Standard-Model Extension (SME) developed since 1997 [8–10]. Aiming to guide experimental searches of Lorentz violation, the SME framework is constructed at the level of effective field theory and treats all possible Lorentz-violating operators as perturbations on top of GR

and the Standard Model. In this work, we study the effects of Lorentz violation on the rotation of stars. This belongs to the gravitational sector of the SME framework, and for simplicity, we only consider the modification to gravity generated by the so-called minimal gravitational SME [11] given by the action

$$S = \frac{1}{16\pi} \int \sqrt{-g}d^4x(R + k^{\alpha\beta\gamma\delta}R_{\alpha\beta\gamma\delta}) + S_k + S_m, \quad (1)$$

where the Ricci scalar R represents the usual Einstein-Hilbert term for GR, $R_{\alpha\beta\gamma\delta}$ is the Riemann tensor, and $k^{\alpha\beta\gamma\delta}$ is the tensor field that breaks local Lorentz invariance when it acquires a nonzero vacuum expectation value in an underlying theory. The action S_k describes the dynamics of the Lorentz-violating field $k^{\alpha\beta\gamma\delta}$ at the level of effective field theory. The symmetry-breaking mechanism is important but generally unspecified [10,12]. One of the central tasks in the gravitational SME is obtaining approximate but general expressions for the contribution of S_k in the field equations using geometric properties of the spacetime manifold like the Bianchi identity and the diffeomorphism invariance [11,13]. The last term S_m is the action of conventional matter and in this work we consider it Lorentz invariant. Note that the geometrized unit system where $G = c = 1$ is used. We will stick to this unit system except when units are specified explicitly. Another explanation of the notations in the remaining of the paper is that repeated indices are summed even when they both are subscripts or superscripts. Also note that the greek letters

*Corresponding author.
xuru@pku.edu.cn
†Corresponding author.
lshao@pku.edu.cn

084028-1

run over spacetime indices, while the latin letters are restricted to spatial indices only.

The weak-field solution of the metric to the field equations obtained from action (1) is calculated by Bailey and Kostelecký [11]. In particular, as the starting point of our study, the anisotropic modification to the Newtonian potential energy between two point particles A and B is

$$\delta U = -\frac{1}{2}\bar{s}^{ij}\frac{m_A m_B}{|\boldsymbol{x}_A - \boldsymbol{x}_B|^3}(x_A^i - x_B^i)(x_A^j - x_B^j), \quad (2)$$

where x_A^i and x_B^i are the components of the position vectors $\boldsymbol{x}_A$ and $\boldsymbol{x}_B$. The quantities $\bar{s}^{ij}$ are defined as the spatial components of

$$\bar{s}^{\alpha\beta} \equiv 2\left(\bar{k}^{\alpha\mu\beta\nu}g_{\mu\nu} - \frac{1}{4}g^{\alpha\beta}\bar{k}^{\lambda\mu\kappa\nu}g_{\mu\nu}g_{\lambda\kappa}\right), \quad (3)$$

with $\bar{k}^{\alpha\beta\gamma\delta}$ being the vacuum expectation value of the tensor field $k^{\alpha\beta\gamma\delta}$ [10]. In practical calculations aiming to test the theoretical predictions against experimental results, the vacuum expectation value $\bar{k}^{\alpha\beta\gamma\delta}$ is taken to be constant around the experimental setting in approximate inertial frames, and its components, as well as the combinations $\bar{s}^{\alpha\beta}$, are called coefficients for Lorentz violation.

Stringent constraints have been set on the SME coefficients for Lorentz violation using an extensive number of laboratory experiments and astrophysical observations [6]. In fact, they include results from considering the effects of Eq. (2) on the rotation of the Sun [11] and two isolated millisecond pulsars [14]. In this work, we consider the two isolated millisecond pulsars in Ref. [14] and set new constraints on the coefficients $\bar{s}^{ij}$. Our work complements the results in the literature as we perform a rigorous study of the rotation of a spheroidal star under the anisotropic gravitational self-energy caused by Eq. (2) to serve as the theoretical basis. In addition, our calculation clarifies the fact that the effect of Lorentz violation adds to stationary spinning stars as well as free-precessing stars. While the former case is the Lorentz-violating precession considered in the literature and has been used to set constraints on the coefficients for Lorentz violation, the latter case has not been investigated to our knowledge. When Lorentz violation modifies the rotation of an otherwise free-precessing neutron star (NS), the pulsar signal and associated continuous gravitational waves (GWs) emitted by the star [15] will change accordingly. A significant part of our work is devoted to this new topic.

Before ending the Introduction, we are obligated to point out that the gravitational sector of the SME is not the only framework to study Lorentz violation in gravity. The celebrated parametrized post-Newtonian (PPN) formalism also includes coefficients describing possible preferred-frame effects in metric gravitational theories [5,16]. The

first study of Lorentz-violating effects on the spins of the Sun and of millisecond pulsars was done by Nordtvedt [17] considering the specific PPN modification[1]

$$\delta U_{\mathrm{PPN}} = \frac{\alpha_2}{2}\frac{m_A m_B}{|\boldsymbol{x}_A - \boldsymbol{x}_B|^3}w^i w^j(x_A^i - x_B^i)(x_A^j - x_B^j) \quad (4)$$

to the Newtonian potential. The coefficient α_2 controls the size of Lorentz violation, while the "absolute" velocity $\boldsymbol{w}$ with respect to the preferred inertial frame picks up a special direction and breaks Lorentz invariance [4]. Our study is originally inspired by Nordtvedt's work [17], and our result recovers his solution when the replacement [11,14]

$$\bar{s}^{ij} \to -\alpha_2 w^i w^j \quad (5)$$

is applied and proper approximations are made. The SME framework is more generic than the PPN formalism in terms of Lorentz violation [11]. Detailed comparisons are presented in relevant paragraphs of the paper.

The organization of the paper is as follows. We start with calculating the anisotropic gravitational self-energy due to Eq. (2) for a spheroidal star in Sec. II A. Then, in Sec. II B, we investigate the solutions to the rotational equations of motion thoroughly, where both the perturbation method and numerical calculation are employed. The observational consequences are discussed in Sec. III with regard to NSs. Section III A considers stationary spinning stars affected by Lorentz violation and obtains constraints on the coefficients for Lorentz violation from the observations of two solitary millisecond pulsars. Sections III B and III C consider free-precessing stars affected by Lorentz violation and provide preliminary signal templates of pulsar pulses and continuous GWs for fitting observational data in the future. Finally, conclusions are summarized in Sec. IV. Appendix displays some expressions for uniform spheroids, which are useful for estimating numerical values.

II. ROTATION OF A SPHEROID UNDER LORENTZ-VIOLATING GRAVITY

A. Anisotropic gravitational self-energy

For a nonspherical star, the integral of the potential energy correction in Eq. (2) depends on the orientation of the star, causing a torque during its rotation. Specifically speaking, we calculate δU in the body frame of the star at any instant,

$$\delta U = -\frac{1}{4}\bar{s}^{ij}\int d^3x d^3x' \rho(\boldsymbol{x})\rho(\boldsymbol{x}')\frac{(x^i - x'^i)(x^j - x'^j)}{|\boldsymbol{x} - \boldsymbol{x}'|^3}, \quad (6)$$

---

[1]Notice that we follow the usage of α_2 by Will [5] related to the one used by Nordtvedt [17] via $\alpha_2 = 2\alpha_2^{\mathrm{Nordtvedt}}$.
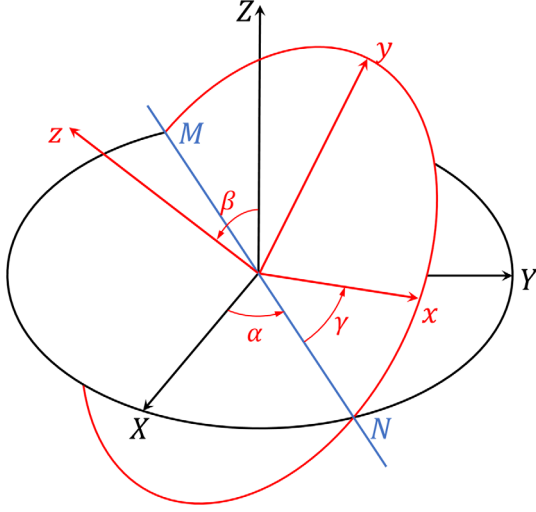
FIG. 1. Euler angles α, β, and γ connecting the $X - Y - Z$ frame and the $x - y - z$ frame. The line MN is the intersection of the X-Y plane and the x-y plane.

where ρ is the density of the star and is assumed to be independent of time in the body frame. The orientation dependence goes into δU as the star rotates. If we set up an inertial frame X-Y-Z, then $\bar{s}^{ij}$ $(i, j = x, y, z)$ in the body frame is related to $\bar{s}^{IJ}$ $(I, J = X, Y, Z)$ in the inertial frame by a rotation transformation

$$\bar{s}^{ij} = R^{iI} R^{jJ} \bar{s}^{IJ}. \tag{7}$$

Noticing that $\bar{s}^{IJ}$ are the constant coefficients for Lorentz violation, δU therefore depends on the orientation of the body through the rotation matrix R^{iI}. The orientation of the body is conveniently described by the Euler angles (see Fig. 1), which are the kinematic quantities to be solved from the equations of motion. For later use, we write the elements of the rotation matrix as

$$R^{iI} = \hat{e}_i \cdot \hat{e}_I, \tag{8}$$

where $\{\hat{e}_i\}$ $(i = x, y, z)$ is the basis of the body frame x-y-z, and $\{\hat{e}_I\}$ $(I = X, Y, Z)$ is the basis of the inertial frame X-Y-Z. The inner products can be computed using the relations [18]

$$
\begin{aligned}
\hat{e}_x &= (\cos\alpha \cos\gamma - \sin\alpha \cos\beta \sin\gamma)\hat{e}_X \\
&\quad + (\sin\alpha \cos\gamma + \cos\alpha \cos\beta \sin\gamma)\hat{e}_Y + \sin\beta \sin\gamma \hat{e}_Z, \\
\hat{e}_y &= (-\cos\alpha \sin\gamma - \sin\alpha \cos\beta \cos\gamma)\hat{e}_X \\
&\quad + (-\sin\alpha \sin\gamma + \cos\alpha \cos\beta \cos\gamma)\hat{e}_Y + \sin\beta \cos\gamma \hat{e}_Z, \\
\hat{e}_z &= \sin\alpha \sin\beta \hat{e}_X - \cos\alpha \sin\beta \hat{e}_Y + \cos\beta \hat{e}_Z.
\end{aligned}
\tag{9}
$$

Back to the potential energy correction in Eq. (6), to proceed with the calculation analytically as much as

possible, we focus on the simple case where the star is a spheroid described by

$$\frac{x^2 + y^2}{a_1^2} + \frac{z^2}{a_3^2} = 1, \tag{10}$$

in the body frame, and its density ρ is axisymmetric about the z axis (for an ellipsoid, see, e.g., Ref. [19]). In such a case, one can show that $\bar{s}^{xy}, \bar{s}^{xz}$, and $\bar{s}^{yz}$ do not appear in δU, and that $\bar{s}^{xx}$ and $\bar{s}^{yy}$ appear as the combination $\bar{s}^{xx} + \bar{s}^{yy}$. Because the trace $\bar{s}^{xx} + \bar{s}^{yy} + \bar{s}^{zz}$ is rotationally invariant and hence does not contribute to the anisotropic correction, the contribution from $\bar{s}^{xx} + \bar{s}^{yy}$ can be represented by $\bar{s}^{zz}$ so that the true anisotropic correction of the potential energy is simply

$$\delta U = C \bar{s}^{zz}, \tag{11}$$

with the constant C being

$$C = \frac{1}{4} \int d^3x \, d^3x' \rho(\boldsymbol{x}) \rho(\boldsymbol{x}') \frac{(x - x')^2 - (z - z')^2}{|\boldsymbol{x} - \boldsymbol{x}'|^3}. \tag{12}$$

The result (11) deserves a comparison with that of Nordtvedt [17]. Treating the potential correction (4) as a perturbation on top of the Newtonian potential, Nordtvedt [17] used the tensor virial relation to obtain the anisotropic gravitational self-energy for a spheroid star as

$$\delta U_{\mathrm{PPN}} = -\frac{1}{2}\alpha_2 T_{\mathrm{rot}} (\boldsymbol{w} \cdot \hat{\boldsymbol{\Omega}})^2, \tag{13}$$

where T_{rot} is the rotational kinetic energy, and $\hat{\boldsymbol{\Omega}}$ is the unit vector along the angular velocity of the star.

First of all, we point out that with the replacement (5), Eq. (11) recovers the form of Eq. (13) when the star spins stationarily along the z axis. As Nordtvedt obtained, for nonrelativistic stars, the constant C is equal to $T_{\mathrm{rot}}/2$ by virtue of the tensor virial relation

$$K^{ij} + \delta^{ij} P - U^{ij} = 0, \tag{14}$$

where δ^{ij} is the Kronecker delta, and

$$
\begin{aligned}
K^{ij} &\equiv \int \rho v^i v^j d^3x, \\
P &\equiv \int p \, d^3x, \\
U^{ij} &\equiv \int \rho x^i \partial_j \Phi d^3x,
\end{aligned}
\tag{15}
$$

with $\boldsymbol{v}$ being the velocity field inside the star, p being the pressure inside the star, and Φ being the usual Newtonian potential

$$\Phi(\pmb{x}) = -\int d^3x' \frac{\rho(\pmb{x}')}{|\pmb{x} - \pmb{x}'|}. \qquad (16)$$

The result $C = T_{\text{rot}}/2$ is straightforward to prove once we notice the integral identity

$$U^{ij} = \frac{1}{2}\int d^3x d^3x' \rho(\pmb{x})\rho(\pmb{x}')\frac{(x^i - x'^i)(x^j - x'^j)}{|\pmb{x} - \pmb{x}'|^3}, \qquad (17)$$

and for a star spinning along the z direction

$$K^{zz} = 0, \qquad T_{\text{rot}} = \frac{1}{2}(K^{xx} + K^{yy}). \qquad (18)$$

In Appendix, the constant C is exhibited for uniform spheroids by utilizing the Newtonian potential inside an ellipsoid of uniform density (see, e.g., Refs. [20,21]).

Second, we notice that Eqs. (11) and (13) are different for a generally rotating spheroidal star whose angular velocity is not aligned with its symmetric axis. The origin of the difference is that Eq. (13) requires the star to be a stationary fluid in equilibrium, while Eq. (11) applies as long as the star has an axisymmetric mass distribution. Whether the star is a fluid or a rigid body does not affect the validity of Eq. (11). Now comes the question: How could the state of the star influence the alignment between its angular velocity and symmetric axis? In fact, if the star is a rigid body, then the direction of its angular velocity can be different from its symmetric axis. But when it is a fluid, the deformation is caused by rotation, and therefore, its symmetric axis must be aligned with its angular velocity as long as the system is in equilibrium.

To better understand the context and the limitation of Eq. (13), let us consider a freely rotating star, namely, when there is no torque. If modeled as a rigid body, depending on whether the angular velocity is aligned with the symmetric axis, two kinds of solutions exist: the stationary spinning solution where the star spins around the fixed symmetric axis, and the free-precessing solution where the star spins around its symmetric axis while that axis rotates around the fixed direction of the conserved angular momentum [18]. If modeled as a fluid, the free-precessing solution cannot exist because even if the angular velocity is not aligned with the symmetric axis initially, the deformation caused by rotation will eventually change the symmetric axis to the direction of angular velocity, leaving the star in the state of stationary spin.

When the torque caused by Lorentz violation is taken into consideration, the two types of solutions for a freely rotating star, namely, the stationary spinning solution and the free-precessing solution, might be treated as the zeroth-order solution for applying the perturbation method. The details are discussed in Sec. II B. Here, we just point out that the effect of the Lorentz-violating torque is forcing the star to precess around one of the principal axes of the $\bar{s}^{ij}$

tensor. When this effect is added to a stationary spinning star, we call the motion *single precession*. When the forced precession due to Lorentz violation is added to a free-precessing star, we call the motion *twofold precession*.

In the single-precession solution, the precession is caused by Lorentz violation, which is assumed to be small. Therefore, the total angular velocity can be approximated as aligned with the symmetric axis of the star. This enables us to put Eq. (11) in the form of Eq. (13) at the leading order of Lorentz violation via the replacement (5). So, the single-precession solution is the one found by Nordtvedt [17]. However, for our result, there is no need to restrict it to fluid stars, as Eq. (11) applies to fluids as well as rigid bodies. The other solution that we defined, the twofold-precession solution, as its name suggests, is a superposition of the free precession where the symmetric axis of the star precesses around the angular momentum and the forced precession where the angular momentum precesses around one of the principal axes of the $\bar{s}^{ij}$ tensor. Though only applicable to stars if they are modeled as rigid bodies, the twofold-precession solution describes a new Lorentz-violating effect in the rotation of stars that has not been studied in the literature to our knowledge.

Before moving to study the solutions in detail, a brief clarification of the model of NS deformation might be useful. We will adopt the model described by Jones and Andersson [22] where the deformation of the star has two contributions: the centrifugal deformation and the Coulomb deformation. The centrifugal deformation is the fluid deformation that scales with the square of the angular velocity, while the Coulomb deformation describes the rigid deviation from the spherical shape sustained by the electrostatic force. The fact that the electrostatic interaction is much weaker than the gravitational interaction in NSs implies that the rigid Coulomb deformation is much smaller than the fluid centrifugal deformation. Using the oblateness defined as

$$\epsilon = \frac{I^{zz} - I^{xx}}{I^{xx}}, \qquad (19)$$

where I^{xx} and I^{zz} are the eigenvalues of the moment of inertia tensor, to characterize the deformations of spheroidal stars, an estimation of the centrifugal deformation is

$$\epsilon_f \approx \frac{|\pmb{\Omega}|^2 R^3}{M} \approx 2.1 \times 10^{-3}\left(\frac{|\pmb{\Omega}|/2\pi}{100\,\text{Hz}}\right)^2\left(\frac{R}{10\,\text{km}}\right)^3\left(\frac{1.4M_\odot}{M}\right), \qquad (20)$$

where $\pmb{\Omega}$ is the angular velocity, R is the radius, and M is the mass of the NS, while the oblateness ϵ_r caused by the Coulomb deformation is about 5 orders of magnitude smaller [22]. Therefore, when applying the single-precession solution to NSs, the rigid deformation ϵ_r can be neglected, and the deformation is described by the fluid

oblateness ϵ_f. However, the fact that NSs can have rigid deformation described by ϵ_r is vital when the twofold-precession solution is to apply. Similar to the free-precessing NSs considered in Refs. [15,22–24], NSs with Lorentz-violating gravity under the twofold-precession produce modulated pulsar signals and in the meantime are sources of continuous GWs providing potential new tests of Lorentz violation. This will be the central topic in Sec. III.

Finally, we point out that Lorentz violation itself also deforms stars [25,26]. But then the deformation due to Lorentz violation contributes at the second order in terms of the coefficients for Lorentz violation to the anisotropic gravitational self-energy. To keep the analysis clear and tractable, we neglect any Lorentz-violating correction to the structure of stars in this work.

B. Rotation of a spheroidal star

We are ready to write down the equations of motion and solve the rotation of a spheroidal star. First, the coefficients for Lorentz violation naturally fix a convenient inertial frame, namely, the one that diagonalizes the $\bar{s}^{IJ}$ matrix. We will use it as the inertial frame X-Y-Z. Please note that the inertial frame widely used in the literature is the canonical Sun-centered celestial-equatorial frame [27]. It is generally different from the frame used here as the off-diagonal coefficients for Lorentz violation unlikely happen to vanish in the canonical Sun-centered celestial-equatorial frame.

With the rotation matrix (8), the anisotropic gravitational self-energy (11) is

$$\delta U = C((\bar{s}^{XX}\sin^2\alpha + \bar{s}^{YY}\cos^2\alpha)\sin^2\beta + \bar{s}^{ZZ}\cos^2\beta), \quad (21)$$

where $\bar{s}^{XX}$, $\bar{s}^{YY}$, and $\bar{s}^{ZZ}$ are the eigenvalues of the $\bar{s}^{IJ}$ matrix. Then, to express the rotational kinetic energy in terms of the Euler angles and their derivatives, we employ the kinematic relation between the velocity components in the body frame and the Euler angles [18],

$$\Omega^x = \dot{\alpha}\sin\beta\sin\gamma + \dot{\beta}\cos\gamma,$$
$$\Omega^y = \dot{\alpha}\sin\beta\cos\gamma - \dot{\beta}\sin\gamma,$$
$$\Omega^z = \dot{\alpha}\cos\beta + \dot{\gamma}, \quad (22)$$

where the dot denotes the time derivative. With $I^{xx} = I^{yy}$, the rotational kinetic energy simplifies to

$$T_{\rm rot} = \frac{1}{2}I^{xx}(\dot{\alpha}^2\sin^2\beta + \dot{\beta}^2) + \frac{1}{2}I^{zz}(\dot{\alpha}\cos\beta + \dot{\gamma})^2. \quad (23)$$

The Euler-Lagrange equations from $L = T_{\rm rot} - \delta U$ can be derived, and there are two first integrals,

$$E = T_{\rm rot} + \delta U,$$
$$\Omega^z = \dot{\alpha}\cos\beta + \dot{\gamma}. \quad (24)$$

The total energy E is not very useful in helping simplify the other equations. The z component of the angular velocity Ω^z can be used to eliminate $\dot{\gamma}$ from the other two Euler-Lagrange equations so that they become

$$\sin^2\beta\ddot{\alpha} + \sin 2\beta\dot{\alpha}\dot{\beta} - \frac{I^{zz}\Omega^z}{I^{xx}}\sin\beta\dot{\beta} = -\frac{1}{I^{xx}}\frac{\partial\delta U}{\partial\alpha},$$
$$\ddot{\beta} - \frac{1}{2}\sin 2\beta\dot{\alpha}^2 + \frac{I^{zz}\Omega^z}{I^{xx}}\sin\beta\dot{\alpha} = -\frac{1}{I^{xx}}\frac{\partial\delta U}{\partial\beta}. \quad (25)$$

First, we consider an illustrative case where only $\bar{s}^{ZZ}$ is nonzero. This is the case where the tensor $\bar{s}^{ij}$ degenerates to a vector as in the correspondence (5). With $\bar{s}^{XX} = \bar{s}^{YY} = 0$, δU is independent of α so that solutions with $\ddot{\alpha} = 0$, $\dot{\beta} = 0$ are consistent with Eqs. (25) given

$$\dot{\alpha} = \frac{I^{zz}\Omega^z \pm \sqrt{(I^{zz}\Omega^z)^2 - 8\bar{s}^{ZZ}CI^{xx}\cos^2\beta}}{2I^{xx}\cos\beta}. \quad (26)$$

When $\bar{s}^{ZZ} = 0$, the "+" sign recovers the free-precessing solution, and the "−" sign gives the stationary spinning solution. Correspondingly, for $\bar{s}^{ZZ} \neq 0$, the + sign gives what we call *twofold precession*, and the − sign gives what we call *single precession*. The single-precession solution, once approximated at the leading order of $\bar{s}^{ZZ} \leftrightarrow -\alpha_2|\mathbf{w}|^2$, is the one obtained by Nordtvedt [17].

The solutions (26) hold when the matrix $\bar{s}^{IJ}$ has only one nonvanishing eigenvalue whose eigenvector is chosen to be the Z axis. Similar solutions exist when the matrix $\bar{s}^{IJ}$ has two same eigenvalues whose eigenvectors are chosen to be the X axis and the Y axis, because in such a case, δU is also independent of α. In fact, a matrix having only one nonvanishing eigenvalue can also be said to have two same eigenvalues where the same eigenvalues are zero. In conclusion, when the matrix $\bar{s}^{IJ}$ has two same eigenvalues, we can set up the X-Y-Z frame properly so that solutions similar to Eq. (26) with a constant β exist.

Now we can discuss the solutions in general when the matrix $\bar{s}^{IJ}$ has three different eigenvalues. In such a case, δU depends on both α and β. Solutions with a constant β do not exist, but as Lorentz violation is supposed to be small, we use the ansatz

$$\alpha = \alpha_0 + at + \alpha^{(1)},$$
$$\beta = \beta_0 + \beta^{(1)} \quad (27)$$

to find perturbative solutions at the leading order of Lorentz violation. In the ansatz (27), α_0 and β_0 are constants, while $\alpha^{(1)}$ and $\beta^{(1)}$ are functions of time assumed to be much smaller than 1. The constant a representing the precessing angular velocity for free rotation takes the values

$$a = \begin{cases} \frac{\omega}{\cos \beta_0}, & \text{free precession,} \\ 0, & \text{stationary spin,} \end{cases} \quad (28)$$

with $\omega \equiv I^{zz}\Omega^z/I^{xx}$ according to Eq. (26) when $\bar{s}^{ZZ} = 0$. Substituting the derivatives of the ansatz (27) into Eqs. (25), and approximating α and β in the equations with $\alpha_0 + at$ and β_0, we find

$$\ddot{\alpha}^{(1)} \pm \frac{\omega}{\sin \beta_0}\dot{\beta}^{(1)} = -\frac{1}{I^{xx}\sin^2\beta_0}\frac{\partial \delta U}{\partial \alpha}\bigg|_{\alpha=\alpha_0+at,\beta=\beta_0},$$

$$\ddot{\beta}^{(1)} \mp \omega \sin \beta_0 \dot{\alpha}^{(1)} = -\frac{1}{I^{xx}}\frac{\partial \delta U}{\partial \beta}\bigg|_{\alpha=\alpha_0+at,\beta=\beta_0}. \quad (29)$$

Note that the upper signs are for the perturbation to a free-precessing star, generating twofold-precession solutions, while the lower signs are for the perturbation to a stationary spinning star, generating single-precession solutions. We will stick to this sign convention when we write expressions containing upper and lower signs. Equations (29) are two coupled oscillation equations for $\dot{\alpha}^{(1)}$ and $\dot{\beta}^{(1)}$ with driven forces. Using Eq. (21) to write out the right-hand sides of Eqs. (29), the solutions can be found as

$$\dot{\alpha}^{(1)} = \mp a^{(1)} \mp \frac{A}{\sin \beta_0}\sin(\omega t + \varphi) + \eta_\alpha \tilde{C}\cos 2(at + \alpha_0),$$

$$\dot{\beta}^{(1)} = A\cos(\omega t + \varphi) + \eta_\beta \tilde{C}\sin 2(at + \alpha_0), \quad (30)$$

with A and φ being two integral constants of the homogeneous solutions. The constants $a^{(1)}$, $\tilde{C}$, η_α, and η_β are

$$a^{(1)} = \frac{C(2\bar{s}^{ZZ} - \bar{s}^{XX} - \bar{s}^{YY})\cos \beta_0}{I^{zz}\Omega^z},$$

$$\tilde{C} = \frac{C(\bar{s}^{XX} - \bar{s}^{YY})}{I^{zz}\Omega^z},$$

$$\eta_\alpha = \begin{cases} \frac{\cos\beta_0(2+\cos^2\beta_0)}{4-\cos^2\beta_0}, & \text{twofold precession,} \\ \cos \beta_0, & \text{single precession,} \end{cases}$$

$$\eta_\beta = \begin{cases} \frac{3\sin\beta_0\cos^2\beta_0}{4-\cos^2\beta_0}, & \text{twofold precession,} \\ \sin \beta_0, & \text{single precession.} \end{cases} \quad (31)$$

We point out that when $\bar{s}^{XX} = \bar{s}^{YY} = 0$, the inhomogeneous solutions in Eqs. (30) recover the solutions (26) at the leading order of Lorentz violation.

The constant $a^{(1)}$, generated by the constant term on the right-hand side of the second equation in Eqs. (29), represents the forced precession due to Lorentz violation. It can be absorbed into a by redefining a to be

$$a = \begin{cases} \frac{\omega}{\cos\beta_0} - a^{(1)}, & \text{twofold precession,} \\ a^{(1)}, & \text{single precession.} \end{cases} \quad (32)$$

Note that the forced precession acts oppositely on a free-precessing star and a stationary spinning star.

Now we can use this new a in solutions (30), and the benefit is that the second term in $\dot{\beta}^{(1)}$ is no longer constant for the single-precession solution. As β at most changes from 0 to π by definition, its rate of change really should not contain any constant term. Keeping in mind that the definition (32) is used, then the ansatz (27) together with the solutions for $\alpha^{(1)}$ and $\beta^{(1)}$,

$$\alpha^{(1)} = \pm\frac{A}{\omega \sin\beta_0}\cos(\omega t + \varphi) + \eta_\alpha\frac{\tilde{C}}{2a}\sin 2(at + \alpha_0),$$

$$\beta^{(1)} = \frac{A}{\omega}\sin(\omega t + \varphi) - \eta_\beta\frac{\tilde{C}}{2a}\cos 2(at + \alpha_0), \quad (33)$$

give the perturbation solutions with integral constants A, φ, α_0, and β_0.

The perturbation solutions are useful in analytically illustrating how Lorentz violation described by the matrix $\bar{s}^{IJ}$ with three different eigenvalues affects a freely rotating spheroidal star. But a complete discussion of the rotational motion has to involve numerical solutions, because there are solutions to Eqs. (25) that cannot be described by the perturbation solutions even at the leading order of Lorentz violation. To see this, let us consider solving Eqs. (25) with initial values given by

$$\alpha|_{t=0} = \alpha_0 \pm\frac{A}{\omega \sin\beta_0}\cos\varphi + \eta_\alpha\frac{\tilde{C}}{2a}\sin 2\alpha_0,$$

$$\beta|_{t=0} = \beta_0 + \frac{A}{\omega}\sin\varphi - \eta_\beta\frac{\tilde{C}}{2a}\cos 2\alpha_0,$$

$$\dot{\alpha}|_{t=0} = a \mp\frac{A}{\sin\beta_0}\sin\varphi + \eta_\alpha\tilde{C}\cos 2\alpha_0,$$

$$\dot{\beta}|_{t=0} = A\cos\varphi + \eta_\beta\tilde{C}\sin 2\alpha_0. \quad (34)$$

The fact that the initial values $\alpha|_{t=0}$, $\beta|_{t=0}$, $\dot{\alpha}|_{t=0}$, and $\dot{\beta}|_{t=0}$ might be arbitrarily assigned indicates that the corresponding integral constants A, φ, α_0, and β_0 should also be able to take any value. However, the perturbative approach restricts A to be small, losing solutions where $\dot{\alpha}|_{t=0}$ is at the order of $\omega/\cos\beta_0$ but significantly different from it. These solutions belong to the case of twofold precession, but because the directions of angular momentum around which free precession happens deviate from the Z axis too much, free precession around the Z axis is no longer able to serve as the zeroth-order solution for the perturbation method. More seriously, the perturbative approach assumes $\alpha^{(1)}$ and $\beta^{(1)}$ to be much smaller than 1. But for the single-precession solution in Eqs. (33), this assumption is very much questionable as a small quantity $a = a^{(1)}$ appears in the denominators of the second terms of $\alpha^{(1)}$ and $\beta^{(1)}$. Somehow, the perturbative single-precession solution does mimic the numerical solutions in one period of the forced
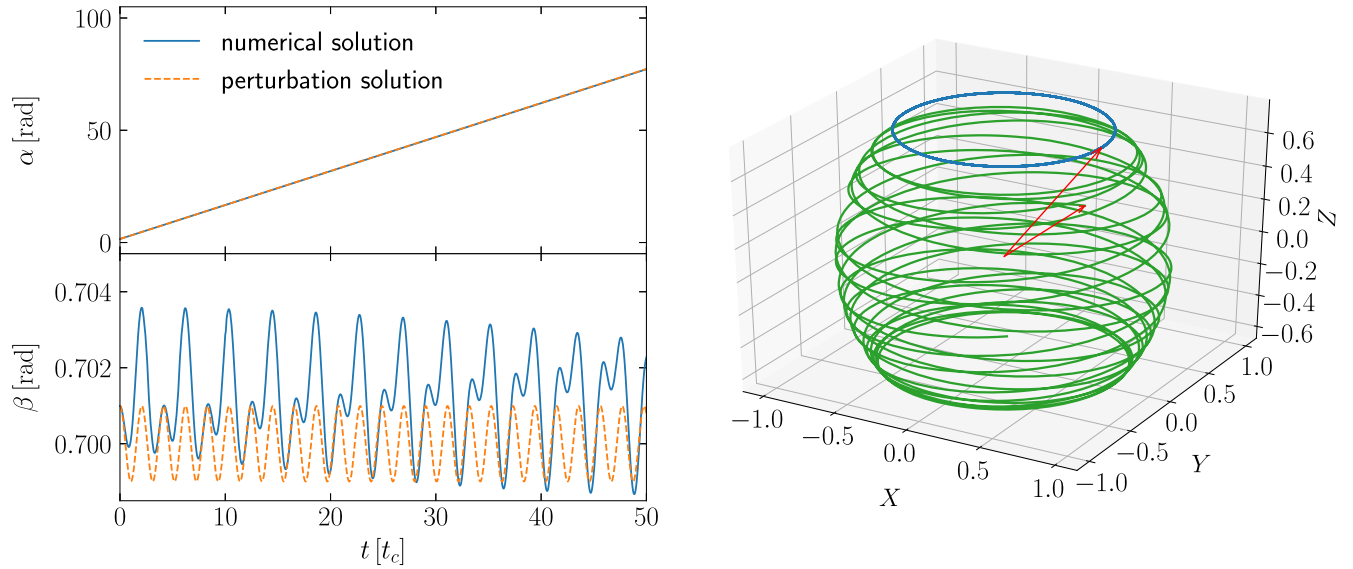
FIG. 2. Example I of twofold precession (denoted as tp-I hereafter). The left plots are the solutions of the Euler angles α and β as functions of time. The right plot shows the trajectories of the heads of $\hat{e}_x$ (green) and $\hat{e}_z$ (blue) in the X-Y-Z frame, while their tails are fixed at the origin. The arrows mark the two vectors at $t = 0$. The initial values $\alpha|_{t=0} = \frac{\pi}{2}$, $\beta|_{t=0} \approx 0.701$, $\dot{\alpha}|_{t=0} \approx 1.509$, and $\dot{\beta}|_{t=0} = 0$ are adopted by setting $\alpha_0 = \frac{\pi}{2}$, $\beta_0 = 0.7$, $A = 0$, and $\varphi = \frac{\pi}{2}$ in Eqs. (34). Other parameters used are $\gamma|_{t=0} = 0$, $\Omega^z = 1$, $I^{zz}/I^{xx} = 1.1$, and $\{\bar{s}^{XX}, \bar{s}^{YY}, \bar{s}^{ZZ}\} = \{0.02, 0.01, -0.04\}$. Time and time derivatives are dimensionless under the time unit t_c defined in Eq. (35).

precession when β_0 is small ($\beta_0 \lesssim 1$). But when β_0 gets close to $\pi/2$, the approximation fails completely.

Figures 2–5 display examples to compare the perturbation solutions with the numerical solutions, and also illustrate the cases where the perturbation method is invalid. In the figures, the time and angular velocities have dimensionless values by employing a time unit t_c defined as

$$t_c = \sqrt{\frac{I^{xx}}{C}}. \tag{35}$$

Then, for demonstration purposes, the integral constant Ω^z is taken to be 1, the ratio I^{zz}/I^{xx} is taken to be 1.1, and the eigenvalues of $\bar{s}^{ij}$ are taken to be $\bar{s}^{XX} = 0.02$, $\bar{s}^{YY} = 0.01$, $\bar{s}^{ZZ} = -0.04$.
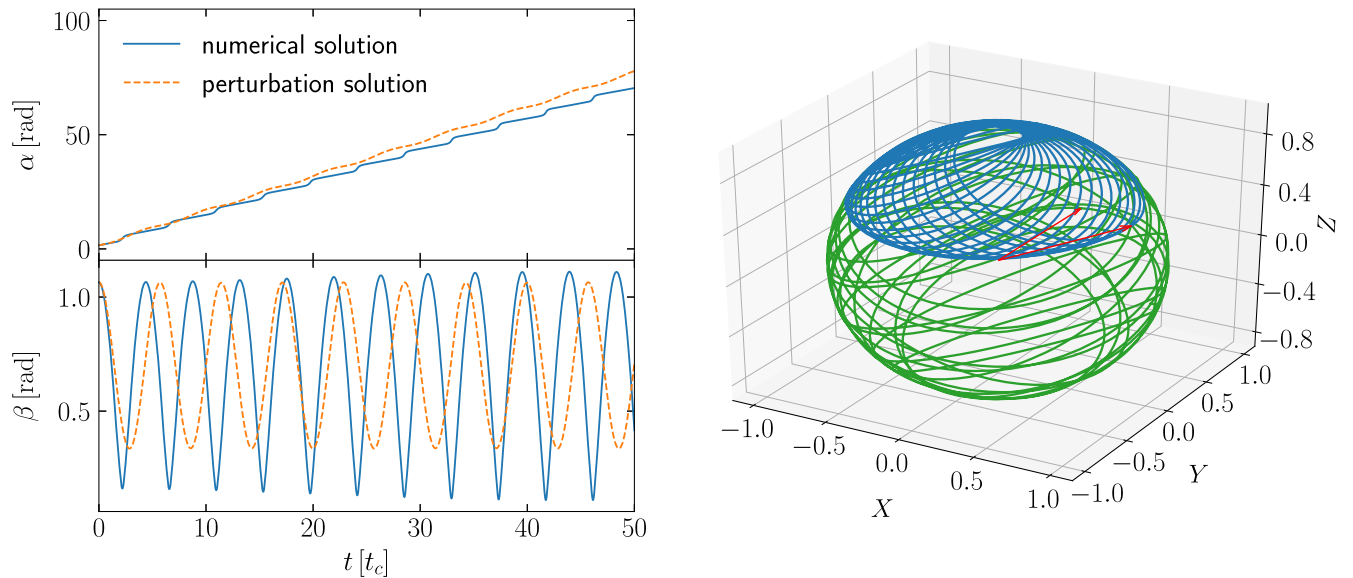

FIG. 3. Example II of twofold precession (denoted as tp-II hereafter). See the caption of Fig. 2 for the meaning of the illustration. The initial values $\alpha|_{t=0} = \frac{\pi}{2}$, $\beta|_{t=0} \approx 1.065$, $\dot{\alpha}|_{t=0} \approx 0.889$, and $\dot{\beta}|_{t=0} = 0$ are adopted by setting $\alpha_0 = \frac{\pi}{2}$, $\beta_0 = 0.7$, $A = 0.4$, and $\varphi = \frac{\pi}{2}$ in Eqs. (34). Other parameters are the same as those in Fig. 2.
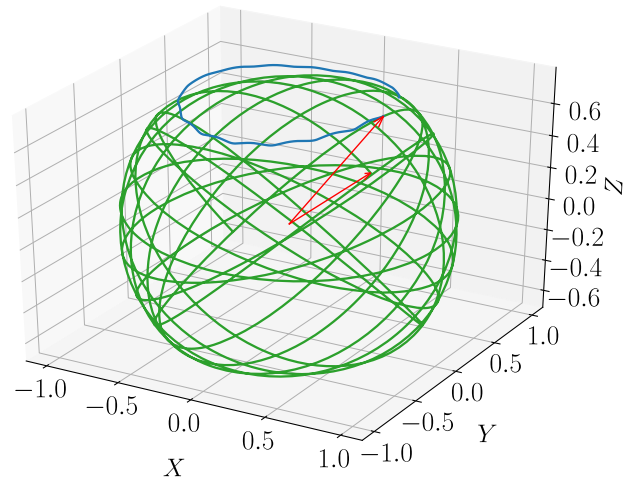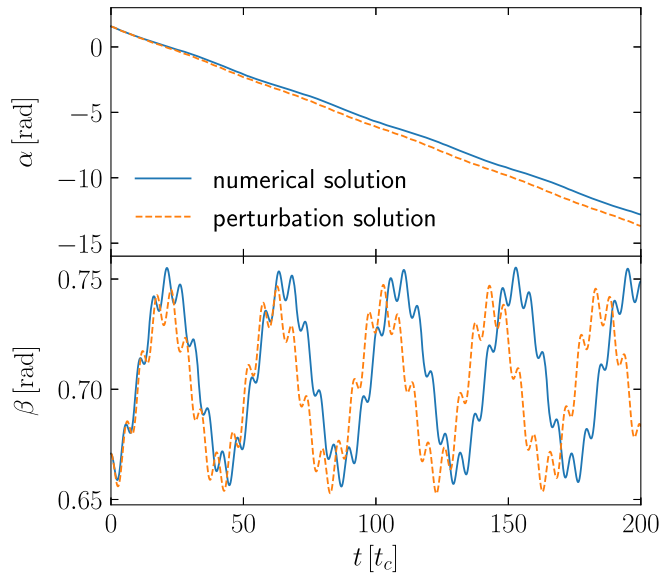
FIG. 4. Example I of single precession. See the caption of Fig. 2 for the meaning of the illustration. The initial values $\alpha|_{t=0} = \frac{\pi}{2}$, $\beta|_{t=0} \approx 0.671$, $\dot{\alpha}|_{t=0} \approx -0.068$, and $\dot{\beta}|_{t=0} = 0$ are adopted by setting $\alpha_0 = \frac{\pi}{2}$, $\beta_0 = 0.7$, $A = 0.01$, and $\varphi = \frac{\pi}{2}$ in Eqs. (34). Other parameters are the same as those in Fig. 2.

Before we turn to the observational consequences, let us address the fact that our discussion above assumes that the forced precession due to Lorentz violation is around the Z axis. Depending on the initial values, the forced precession can be around the other two principal axes of the matrix $\bar{s}^{IJ}$. An interesting result from our study of the numerical solutions is that without loss of generality, if the three different eigenvalues of $\bar{s}^{ij}$ satisfy $\bar{s}^{ZZ} < \bar{s}^{YY} < \bar{s}^{XX}$, then

the forced precession around the Y axis is unstable. This is very similar to the Dzhanibekov effect (also called the tennis racket theorem) in free rotation [28]. Once this is stated, we point out that the above discussion equally applies to the forced precession around the X axis by changing the indices

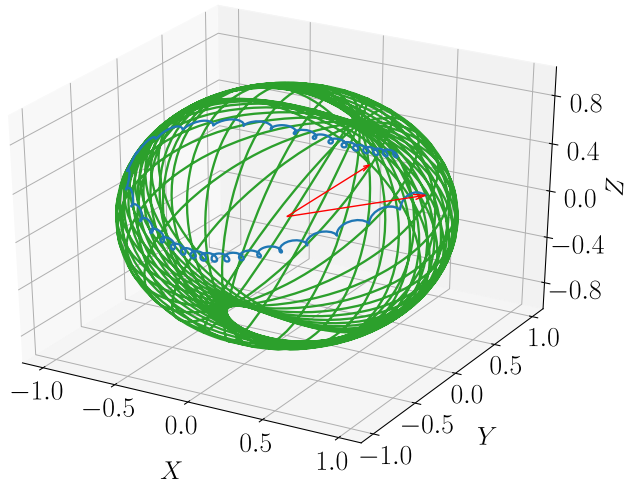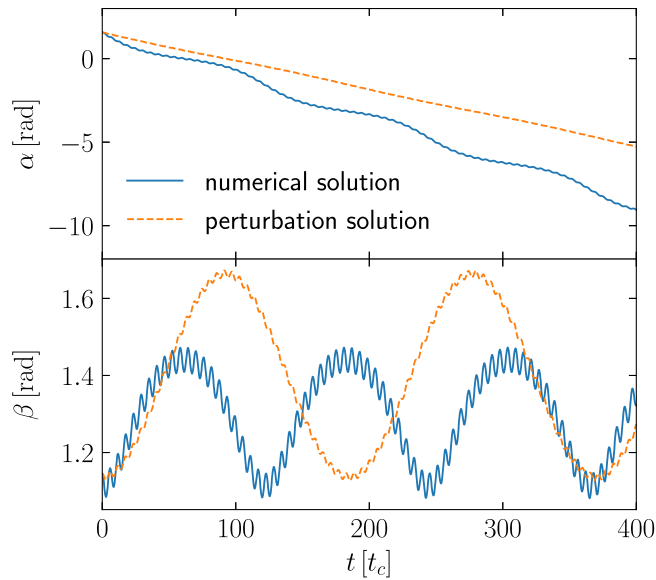$$Z \to X, \qquad X \to Y, \qquad Y \to Z \qquad (36)$$

FIG. 5. Example II of single precession. See the caption of Fig. 2 for the meaning of the illustration. The initial values $\alpha|_{t=0} = \frac{\pi}{2}$, $\beta|_{t=0} \approx 1.146$, $\dot{\alpha}|_{t=0} \approx -0.008$, and $\dot{\beta}|_{t=0} = 0$ are adopted by setting $\alpha_0 = \frac{\pi}{2}$, $\beta_0 = 1.4$, $A = 0.01$, and $\varphi = \frac{\pi}{2}$ in Eqs. (34). Other parameters are the same as those in Fig. 2.
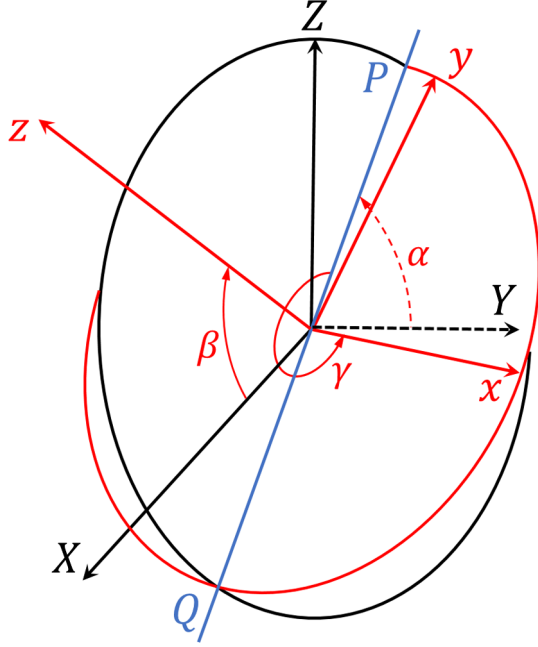
FIG. 6. Euler angles α, β, and γ connecting the Y-Z-X frame and the x-y-z frame. The line PQ is the intersection of the Y-Z plane and the x-y plane.

in Eqs. (31) and keeping in mind that (α, β, γ) now refer to the Euler angles between the x-y-z frame and the Y-Z-X frame (see Fig. 6).

III. OBSERVATIONAL CONSEQUENCES

NSs observed as pulsars provide tests against the above-predicted single-precession motion due to Lorentz-violating gravity [14,17,29,30]. In Sec. III A, we will discuss the constraints set on the coefficients for Lorentz violation by applying the single-precession solution to two observed solitary millisecond pulsars [29]. On the other hand, the twofold-precession solution, developed from free precession once Lorentz-violating gravity presents, cannot be used to constrain the coefficients for Lorentz violation currently as evidence of free-precessing NSs are yet preliminary (see, e.g., Ref. [31]). Based on the hypothesis that NSs might possess tiny rigid deformations, the modulations on pulsar signals and the emission of continuous GWs due to free precession have been studied in the literature to predict observational signatures for searching such NSs [15,22–24]. Following similar considerations, we investigate in Secs. III B and III C the observational signatures in pulsar pulses and continuous GW signals from NSs undergoing the twofold-precession motion.

A. Single-precession motion and constraints on Lorentz violation

We start with considering the change of the angle between the spin axis $\hat{e}_z$ and a fixed direction in the

X-Y-Z frame when a star is in the state of single precession. Calling that angle λ and describing the fixed direction using the spherical angular coordinates (θ_o, ϕ_o) in the X-Y-Z frame, we have the relation

$$\cos\lambda = \sin\theta_o \sin\beta \sin(\alpha - \phi_o) + \cos\theta_o \cos\beta, \quad (37)$$

where α and β are the Euler angles used in Sec. II. Assume that the changes in α and β are much smaller than 1 during a certain time interval, then the change of $\cos\lambda$ can be approximated as

$$\Delta\cos\lambda \approx (\sin\theta_o \cos\beta \sin(\alpha - \phi_o) - \cos\theta_o \sin\beta)\Delta\beta$$
$$+ \sin\theta_o \sin\beta \cos(\alpha - \phi_o)\Delta\alpha. \quad (38)$$

For estimations, we use the perturbation solution (27) to approximate the changes in α and β as

$$\Delta\alpha \approx \dot{\alpha}\Delta t \approx \left(1 + \frac{A}{a^{(1)}\sin\beta_0}\sin\varphi + \frac{\cos\beta_0 \tilde{C}}{a^{(1)}}\cos 2\alpha_0\right)a^{(1)}\Delta t,$$

$$\Delta\beta \approx \dot{\beta}\Delta t \approx \left(\frac{A}{a^{(1)}}\cos\varphi + \frac{\sin\beta_0 \tilde{C}}{a^{(1)}}\sin 2\alpha_0\right)a^{(1)}\Delta t, \quad (39)$$

where the start of the time interval Δt has been set at $t = 0$. Because A, $\tilde{C}$, and $a^{(1)}$ are at the same order, $\Delta\alpha$, $\Delta\beta$, and hence, $\Delta\cos\lambda$ are proportional to $a^{(1)}\Delta t$ with factors of order unity. Here we neglect any situation where (θ_o, ϕ_o) and $\{A, \varphi, \alpha_0, \beta_0\}$ are fine-tuned to vanish the factor for $\Delta\cos\lambda$. Once an observation puts a bound on the change of λ during a certain time interval, the corresponding constraint on the combination $2\bar{s}^{ZZ} - \bar{s}^{XX} - \bar{s}^{YY}$ is

$$|2\bar{s}^{ZZ} - \bar{s}^{XX} - \bar{s}^{YY}| \lesssim \left|\frac{I^{zz}\Omega^z}{C\Delta t \cos\beta_0}\Delta\cos\lambda\right|. \quad (40)$$

The estimation (40) depends on β_0, which roughly characterizes the angle between the symmetric axis of the star and the Lorentz-violating principal axis around which the forced precession happens. Checked with numerical results, we find that when $\beta_0 \lesssim 1.1$, the estimation (40) gives correct orders of magnitude for $|2\bar{s}^{ZZ} - \bar{s}^{XX} - \bar{s}^{YY}|$. But as we mentioned in Sec. II B, when β_0 approaches $\pi/2$, the estimation (40) fails because the perturbation method breaks down. A semianalytical relation based on Eq. (40) and numerical results is

$$|2\bar{s}^{ZZ} - \bar{s}^{XX} - \bar{s}^{YY}| \lesssim \eta\left|\frac{I^{zz}\Omega^z}{C\Delta t}\Delta\cos\lambda\right|, \quad (41)$$

where η can be approximated by $1/\cos\beta_0$ for $\beta_0 \lesssim 1.1$ but then only increases to 10 when β_0 approaches $\pi/2$.

Now we are ready to apply Eq. (41) to two solitary pulsars: PSRs B1937 + 21 and J1744 − 1134. Their observed pulse profiles over 15 years were thoroughly

TABLE I. Observational quantities from PSRs B1937 + 21 and J1744 − 1134 [29] to constrain Lorentz violation. The pulse profile of PSR B1937 + 21 consists of a main pulse and an interpulse, both of which put bounds on the change of λ and hence constrain Lorentz violation. The pulse width is taken at 50% intense level in practice. The last row, conservative bound on $|2\bar{s}^{ZZ} - \bar{s}^{XX} - \bar{s}^{YY}|$, is obtained by setting $\eta = 10$.

	Main pulse of PSR B1937 + 21	Interpulse of PSR B1937 + 21	PSR J1744 − 1134
Spin period (ms)	1.6	1.6	4.1
W (deg)	8.3	10	13
Bound on ΔW (10^{-3} deg)	−48	53	20
λ (deg)	100	100	95
χ (deg)	75	105	51
Bound on $\Delta\lambda$ (10^{-3} deg)	−19	−5.2	1.6
Bound on $|2\bar{s}^{ZZ} - \bar{s}^{XX} - \bar{s}^{YY}|$	$10^{-14}\eta$	$10^{-15}\eta$	$10^{-16}\eta$
Conservative bound on $|2\bar{s}^{ZZ} - \bar{s}^{XX} - \bar{s}^{YY}|$	10^{-13}	10^{-14}	10^{-15}

analyzed by Shao *et al.* [29]. Here we simply use the conclusion that the change in the angle λ, now being the angle between the spin axis and the line of sight, is bounded by

$$\Delta\lambda = \frac{1}{2}\frac{\sin\frac{W}{2}}{\cot\lambda\cos\frac{W}{2} + \cot\chi}\Delta W, \quad (42)$$

where W is the pulse width, ΔW is the change in W during the 15 years, and χ is the angle between the spin axis of the NS and the symmetric axis of the pulsar beam which has been assumed to take the shape of a narrow cone [32]. The values of those quantities for each pulsar are listed in Table I. The derived bounds on $\Delta\lambda$ and hence on the combination $|2\bar{s}^{ZZ} - \bar{s}^{XX} - \bar{s}^{YY}|$ are shown in the last three rows of the table (the last row is the same as the second to last row except that η is set to 10, which is suggested as the upper limit of η by our numerical solutions). As an estimation, a uniform density of $\rho_{NS} \sim 10^{15}$ g/cm^3 and a fluid deformation of $\epsilon_f \sim 10^{-3}$ have been used to get

$$\frac{I^{zz}}{C} \approx \frac{15}{4\pi}\frac{1}{\rho_{NS}\epsilon_f} \sim 10^{-5} \text{ s}^2 \quad (43)$$

for the NSs.

Under the correspondence (5), the constraints in Table I are consistent with those in Ref. [29] for the PPN α_2 parameter. Then, we do notice that they are 3 to 5 orders of magnitude better than the *global* results in Ref. [14] where the same two solitary pulsars were used, but the test was done together with another 11 binary pulsars in order to obtain the global constraints on the coefficients for Lorentz violation instead of the "maximal-reach" ones as done in Ref. [33]. This shows that, (i) observations of solitary pulsars are more sensitive to Lorentz violation than those of binary pulsars, and (ii) the correlations between different coefficients for Lorentz violation can severely degrade the constraints [14].

B. Twofold-precession motion and pulsar signal

To construct pulsar signals from a NS under the twofold-precession motion, we adopt the cone model to describe the radiation beam [32,34]. Figure 7 illustrates a half radiation cone in the X-Y-Z frame. In principle, the radiation comes from two opposite sides of a NS and is in the shape of a double cone. But for clarity, we will only track the half cone as shown in Fig. 7 and analyze the signal from it. The signal from the opposite half cone can be obtained simply by reversing the unit vector along the axis of the cone in the following analysis.

In the cone model, signals are observed when the line of sight is inside the radiation cone. Mathematically, it means
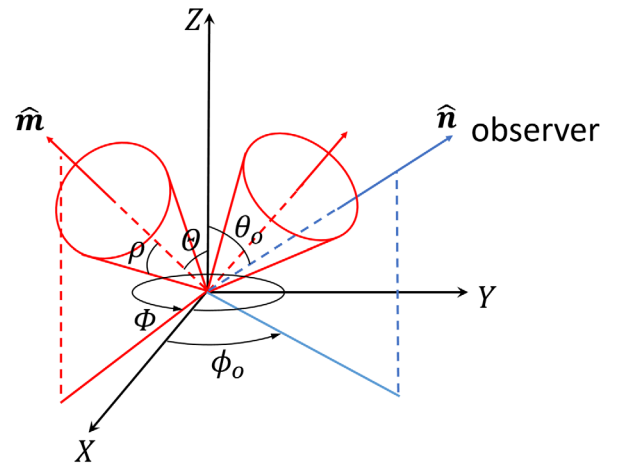

FIG. 7. Cone model for pulsar radiation [32,34]. The unit vector along the magnetic dipole moment is denoted as $\hat{m}$. It is the symmetric axis of the cone. The semiopen angle of the cone is denoted as ρ. While the star rotates, $\hat{m}$ changes its orientation, and at some time, the cone encloses a unit vector $\hat{n}$, so the radiation is received by the observer in the direction of $\hat{n}$. The colatitude and the azimuth for $\hat{m}$ and $\hat{n}$ in the X-Y-Z frame are denoted as (Θ, Φ) and (θ_o, ϕ_o), respectively.

$$\cos\rho < \hat{\boldsymbol{m}} \cdot \hat{\boldsymbol{n}}, \tag{44}$$

where ρ is the semiopen angle of the cone, $\hat{\boldsymbol{m}}$ is the unit vector along the axis of the cone, and $\hat{\boldsymbol{n}}$ is the unit vector along the line of sight. The axis of the cone, generally believed to be aligned with the magnetic dipole moment of the star, is fixed in the body frame and therefore can be described by two constant angular coordinates (χ, δ) as

$$\hat{\boldsymbol{m}} = \sin\chi \cos\delta \hat{\boldsymbol{e}}_x + \sin\chi \sin\delta \hat{\boldsymbol{e}}_y + \cos\chi \hat{\boldsymbol{e}}_z. \tag{45}$$

The direction of the line of sight, if we neglect the proper motion of the star relative to the observer, is fixed in the X-Y-Z frame and will be described by two constant angular coordinates (θ_o, ϕ_o) as

$$\hat{\boldsymbol{n}} = \sin\theta_o \cos\phi_o \hat{\boldsymbol{e}}_X + \sin\theta_o \sin\phi_o \hat{\boldsymbol{e}}_Y + \cos\theta_o \hat{\boldsymbol{e}}_Z. \tag{46}$$

Using Eqs. (9), the product of $\hat{\boldsymbol{m}}$ and $\hat{\boldsymbol{n}}$ can be written as a function of time due to the time-dependent Euler angles,

$$\begin{aligned}
\hat{\boldsymbol{m}} \cdot \hat{\boldsymbol{n}} = {} & \sin\theta_o \sin\chi \cos(\alpha - \phi_o) \cos(\gamma + \delta) \\
& - \sin\theta_o \sin\chi \sin(\alpha - \phi_o) \cos\beta \sin(\gamma + \delta) \\
& + \sin\theta_o \cos\chi \sin(\alpha - \phi_o) \sin\beta \\
& + \cos\theta_o \sin\chi \sin\beta \sin(\gamma + \delta) \\
& + \cos\theta_o \cos\chi \cos\beta.
\end{aligned} \tag{47}$$

The angles ϕ_o and δ can be absorbed into the initial values of α and γ in the above expression. For given θ_o, χ, and ρ, once the rotation of the star is known, the inequality (44) can be solved to predict the time intervals during which signals are observed.

A quick review of the observational signatures of free-precessing pulsars is heuristic to explore the twofold-precession case; more details can be found in, e.g., Ref. [15]. For an axisymmetric NS, the free-precessing solution has

$$\begin{aligned}
\dot{\alpha} &= \frac{I^{zz}\Omega^z}{I^{xx}\cos\beta}, \\
\dot{\gamma} &= \Omega^z - \dot{\alpha}\cos\beta = -\epsilon\Omega^z,
\end{aligned} \tag{48}$$

with the angle β being constant. Therefore, the expression $\hat{\boldsymbol{m}} \cdot \hat{\boldsymbol{n}}$ as shown in Eq. (47) is simply a sum of four sinusoids of angular frequencies $\dot{\alpha} - \dot{\gamma}$, $\dot{\alpha}$, $\dot{\alpha} + \dot{\gamma}$, and $\dot{\gamma}$. The analysis is further simplified by the fact that the deformation ϵ is extremely small for NSs so that the frequency components $\dot{\alpha} \pm \dot{\gamma}$ are basically the same as $\dot{\alpha}$, leaving the pulsar period to be $P \approx 2\pi/\dot{\alpha}$ and modulated with a period of $P_P \approx 2\pi/|\dot{\gamma}|$. Here we assume that the directions of the z axis and the Z axis are properly chosen so that Ω^z and $\cos\beta$ are positive.

An exact analytical expression of the pulsar period P in terms of the Euler angles was derived in Ref. [22] by calculating the rate of the azimuthal angle of $\hat{\boldsymbol{m}}$ in the X-Y-Z frame. Denote the angular coordinates of $\hat{\boldsymbol{m}}$ in the X-Y-Z frame as (Θ, Φ), then their relation with (χ, δ) can be found by transforming the Cartesian components of $\hat{\boldsymbol{m}}$ under the rotation (8). The result is

$$\begin{aligned}
\cos\Theta &= \cos\beta \cos\chi + \sin\beta \sin\chi \sin(\gamma + \delta), \\
\tan\Phi &= \tan(\alpha + \Delta\Phi),
\end{aligned} \tag{49}$$

where

$$\tan\Delta\Phi = \frac{\cos\beta \sin(\gamma + \delta) - \sin\beta \cot\chi}{\cos(\gamma + \delta)}. \tag{50}$$

The pulsar period defined as the time intervals between $\hat{\boldsymbol{m}}$ consecutively passing through the plane formed by the Z axis and the observer is then

$$P \equiv \frac{2\pi}{\dot{\Phi}} = \frac{2\pi}{\dot{\alpha} + \Delta\dot{\Phi}} \approx \frac{2\pi}{\dot{\alpha}}\left(1 - \frac{\Delta\dot{\Phi}}{\dot{\alpha}}\right), \tag{51}$$

where

$$\Delta\dot{\Phi} = -\dot{\gamma}\frac{\sin\beta \cot\chi \sin(\gamma + \delta) - \cos\beta}{\cos^2(\gamma + \delta) + (\sin\beta \cot\chi - \cos\beta \sin(\gamma + \delta))^2}. \tag{52}$$

Equation (51) not only confirms that the pulsar period P is approximately generated by the angular frequency $\dot{\alpha}$ and that the modulation on P involves sinusoidal functions of γ, but also describes the time evolution of P quantitatively, ready to fit observational data, say, to extract the parameters $\dot{\alpha}$, $\dot{\gamma}$, β, and χ.

Besides the pulsar period, the widths of pulse signals also encode information on the motion of the star. With the cone model of the radiation beam, it is defined as the change of the azimuthal angle of $\hat{\boldsymbol{m}}$ in the X-Y-Z frame during the time when $\hat{\boldsymbol{n}}$ is inside the cone, namely,

$$W \equiv \Phi_2 - \Phi_1, \tag{53}$$

where Φ_1 and Φ_2 are the azimuthal angle Φ solved from the equation of the inequality (44) with

$$\hat{\boldsymbol{m}} \cdot \hat{\boldsymbol{n}} = \sin\Theta \sin\theta_0 \cos(\Phi - \phi_o) + \cos\Theta \cos\theta_o. \tag{54}$$

Fortunately, because $|\dot{\gamma}|$ is much smaller than $\dot{\Phi} \approx \dot{\alpha}$, the angle Θ given by the first equation in Eqs. (49) can be treated as unchanged during Φ changing from Φ_1 to Φ_2 so that the roots Φ_1 and Φ_2 are symmetric about the azimuthal angle ϕ_o of the observer, namely,
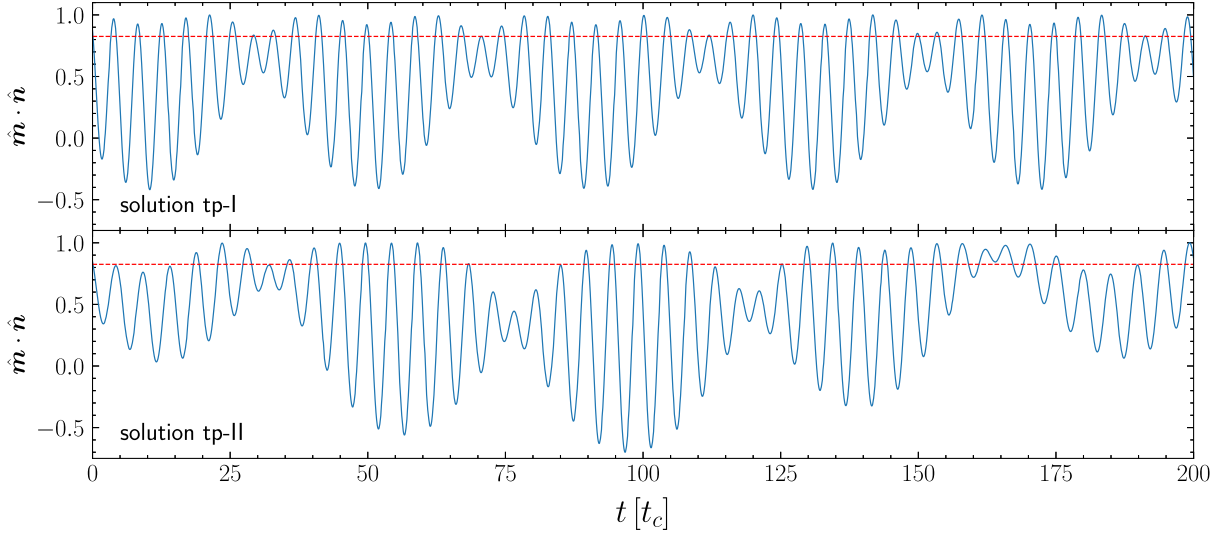
FIG. 8. Time evolutions of $\hat{\boldsymbol{m}} \cdot \hat{\boldsymbol{n}}$ using the numerical solutions in Figs. 2 and 3. The constant angles θ_o and χ are taken to be 0.8 and 0.5 rad in the plots. The red dashed lines represent the cosine value of $\rho = 0.6$ rad, illustrating the time segments when $\hat{\boldsymbol{m}} \cdot \hat{\boldsymbol{n}}$ is above $\cos \rho$ so that the signal is observed under the corresponding setup. With our choice of $\epsilon_r = 0.1$ in the numerical solutions, the time unit is $t_c \sim 10^{-3}$ s if the density of the NS is $\rho_{\mathrm{NS}} \sim 10^{15}$ g/cm^3.

$$\Phi_1 \approx \phi_o - \frac{W}{2}, \qquad \Phi_2 \approx \phi_o + \frac{W}{2}, \qquad (55)$$

and hence, as given in Refs. [32,34], setting the expression (54) equal to $\cos \rho$ leads to an analytical expression for W,

$$\cos \frac{W}{2} \approx \frac{\cos \rho - \cos \Theta \cos \theta_o}{\sin \Theta \sin \theta_o}. \qquad (56)$$

When the time dependence of Θ is put back in Eq. (56), it describes the modulated pulse width at the period $P_P \approx 2\pi/|\dot{\gamma}|$. By fitting this equation to observational data, the parameters $\dot{\gamma}$, ρ, and θ_o can be extracted.

Let us now turn to the Lorentz-violating twofold-precession case. Similar characteristics of pulse signals exist. In fact, Eqs. (51) and (56) apply straightforwardly as long as $|\dot{\gamma}| \ll \dot{\alpha}$. This is exactly the regime where the perturbation solution of the twofold precession works. Neglecting the oscillating terms $\alpha^{(1)}$ and $\beta^{(1)}$, the perturbation solution has

$$\dot{\alpha} \approx a = \frac{I^{zz} \Omega^z}{I^{xx} \cos \beta_0} - a^{(1)},$$

$$\dot{\gamma} = \Omega^z - \dot{\alpha} \cos \beta \approx -\epsilon \Omega^z + \cos \beta_0 a^{(1)}, \qquad (57)$$

where the free-precessing angular frequencies $\dot{\alpha}$ and $\dot{\gamma}$ are shifted due to Lorentz violation. By fitting Eqs. (51) and (56) to observational data, we will be able to extract the two shifted frequencies $\dot{\alpha}$ and $\dot{\gamma}$ and the angular parameters β_0, χ, ρ, and θ_o.

A crucial defect here is that once $\dot{\alpha}$ and $\dot{\gamma}$ are extracted, we are unable to deduce Ω^z, ϵ, and $a^{(1)}$ simultaneously. One

more piece of information on the three quantities is required from the observational data. It involves details of the pattern of $\hat{\boldsymbol{m}} \cdot \hat{\boldsymbol{n}}$ that are beyond the perturbation approximation of $\dot{\alpha}$ and $\dot{\gamma}$ in Eqs. (57), and inevitably invokes numerical solutions of the twofold-precession motion. Numerical calculations for $\hat{\boldsymbol{m}} \cdot \hat{\boldsymbol{n}}$ are also necessary for another important reason. When $\dot{\gamma}$ is not much smaller than $\dot{\alpha}$, the perturbation solution breaks down, and to make matters worse, Eqs. (51) and (56) are also not valid anymore, so there are no analytical templates to fit the pulsar period and the pulse width. In this case, the inequality (44) needs to be solved numerically to deduce the discrete time series of the pulsar period and pulse width to fit the observational data. The rotation of the star, the parameters ϵ, χ, ρ, and θ_o, and the coefficients for Lorentz violation $\bar{s}^{XX}$, $\bar{s}^{YY}$, and $\bar{s}^{ZZ}$ might be determined via elaborate numerical calculations and careful treatments. Of course, other measurements, like the polarization properties of the radiation, might provide extra information and can be combined to derive a full solution. This is beyond the scope of the current work.

In Fig. 8, the time evolutions of $\hat{\boldsymbol{m}} \cdot \hat{\boldsymbol{n}}$ using the two numerical solutions in Fig. 2 (solution tp-I) and Fig. 3 (solution tp-II) are displayed, while Fig. 9 depicts the corresponding angular frequency spectra. A decisive characteristic shows up in the case of the solution that invalidates the perturbation approach (namely, solution tp-II). That is the extra smallest frequency component appearing in the lower plot of Fig. 9. This frequency corresponds to the average angular velocity at which the angular momentum of the star precesses about the Z axis. Though no simple approximate expression relates it to the coefficients for Lorentz violation, numerical calculations indicate that this
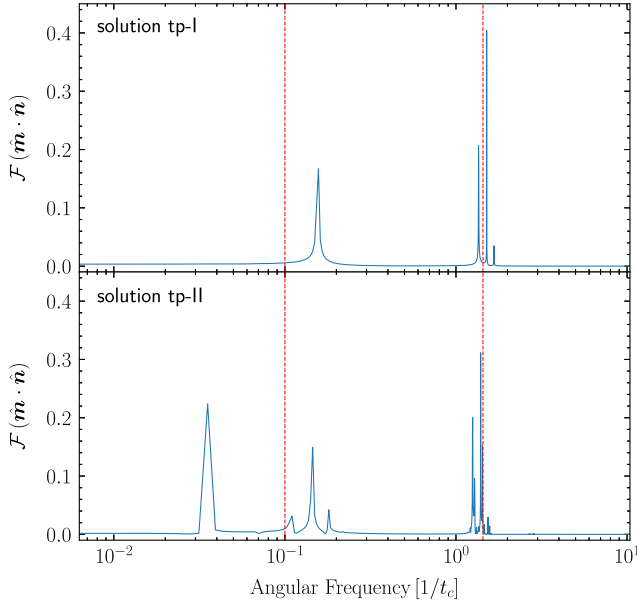
FIG. 9. Fourier transformations for $\hat{\boldsymbol{m}} \cdot \hat{\boldsymbol{n}}$ in Fig. 8. The dashed red vertical lines mark $\dot{\alpha} \approx 1.438$ and $|\dot{\gamma}| = 0.1$, which are the values from the free-precessing equations (48) with $I^{zz}/I^{xx} = 1.1$, $\Omega^z = 1$, and $\beta = 0.7$. As we have taken $\epsilon_r = 0.1$, the frequency unit is $1/t_c \sim 1000$ rad/s if the density of the NS is $\rho_{\mathrm{NS}} \sim 10^{15}$ g/cm³.

angular frequency has the same order of magnitude as the coefficients for Lorentz violation under the dimensionless parametrization using the time unit defined in Eq. (35), which for realistic NSs has an estimation

$$t_c \approx \sqrt{\frac{15}{4\pi} \frac{1}{\rho_{\mathrm{NS}} \epsilon_r}} \sim 1 \text{ s}, \tag{58}$$

with density $\rho_{\mathrm{NS}} \sim 10^{15}$ g/cm³ and rigid deformation $\epsilon_r \sim 10^{-8}$ assumed.[2] The extra frequency component does not show up in the case of solution tp-I, because in that case, the angular momentum of the star is almost aligned with the Z axis, so the precession of the angular momentum around the Z axis caused by Lorentz violation degenerates with the free precession, generating a total precession rate $\dot{\alpha}$ approximately given by the first equation in Eqs. (57) where the Lorentz-violating contribution $a^{(1)}$ is unable to be decoupled.

In Fig. 10, the discrete time series of the pulsar period and of the time segment corresponding to the pulse width calculated by solving the inequality (44) using the numerical templates of $\hat{\boldsymbol{m}} \cdot \hat{\boldsymbol{n}}$ from Fig. 8 are plotted. For the case of the solution tp-I (left panels of Fig. 10), the smooth curves that approximate the discrete points are generated

---

[2]We must point out that because we use $I^{zz}/I^{xx} = 1.1$ for illustrative purposes in our numerical examples, meaning $\epsilon_r = 0.1$, the time unit t_c in the plots is really at the order of 10^{-3} s if the density is $\rho_{\mathrm{NS}} \sim 10^{15}$ g/cm³.

using Eqs. (51) and (56). They fit very well. For the case of the solution tp-II (right panels of Fig. 10), Eqs. (51) and (56) fail to approximate the discrete series, so we have to interpolate the points to reveal their trends. Note that in both cases there is a period of about $40 t_c$ originated from the angular frequency between $0.1 t_c^{-1}$ and $0.2 t_c^{-1}$ in Fig. 9, while in the right panels, a period of about $180 t_c$ shows up—more perceivable in the pulsar-period plot than in the pulse-width plot—reflecting the characteristic angular frequency between $0.03 t_c^{-1}$ and $0.04 t_c^{-1}$ in the lower panel of Fig. 9.

C. Twofold-precession motion and continuous GWs

The quadrupole GW radiated by a freely precessing rigid body was calculated in Refs. [23,35]. To investigate the quadrupole radiation by a rigid body undergoing the twofold-precession motion due to Lorentz violation, we generalize Zimmermann's calculation [35] to any rotating rigid body with torques.

The metric perturbation in the X-Y-Z frame is given by the quadrupole formula

$$h^{IJ} = -\frac{2}{r} \ddot{I}^{IJ}, \tag{59}$$

where r is the distance from the star to the observer, and the double dots denote the second time derivative. The time dependence of the inertial-frame components of the moment of inertia tensor originates in the rotation matrix via

$$I^{IJ} = R^{iI} R^{jJ} I^{ij}, \tag{60}$$

while the body-frame components of the moment of inertia tensor are constant. The derivatives of R^{iI} can be derived by noticing that the body-frame axes undergo an infinitesimal rotation

$$\hat{\boldsymbol{e}}_i \rightarrow \hat{\boldsymbol{e}}_i + dt \boldsymbol{\Omega} \times \hat{\boldsymbol{e}}_i \tag{61}$$

at the instant when the body rotates with an angular velocity $\boldsymbol{\Omega}$. The change of R^{iI} is therefore $dt(\boldsymbol{\Omega} \times \hat{\boldsymbol{e}}_i) \cdot \hat{\boldsymbol{e}}_I$, giving

$$\frac{dR^{iI}}{dt} = (\boldsymbol{\Omega} \times \hat{\boldsymbol{e}}_i) \cdot \hat{\boldsymbol{e}}_I = \epsilon^{IJK} \Omega^J R^{iK}, \tag{62}$$

where ϵ^{IJK} is the Levi-Civita symbol. Equation (62) can be used to calculate $\dot{I}^{IJ}$. When combined with the equation of motion

$$\dot{I}^{IJ} \Omega^J + I^{IJ} \dot{\Omega}^J = \Gamma^I, \tag{63}$$

$\dot{\boldsymbol{\Omega}}$ can be solved in terms of $\boldsymbol{\Omega}$ and the torque $\boldsymbol{\Gamma}$. Then, the demanded second derivative $\ddot{I}^{IJ}$ can be found to take the form
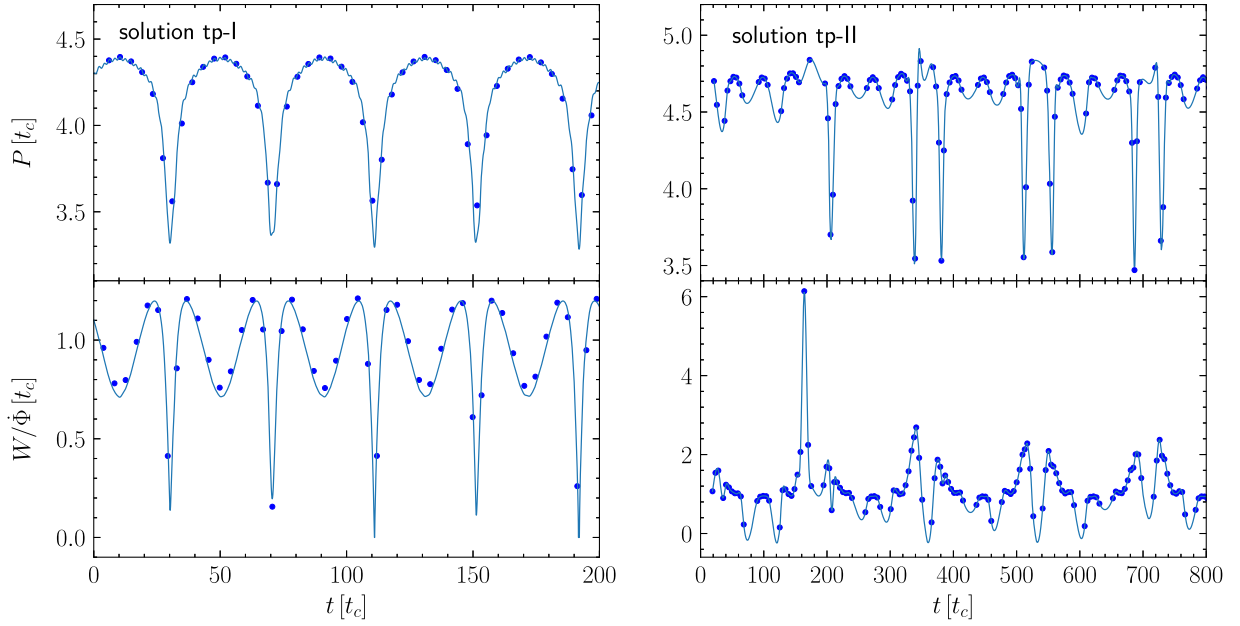
$$\ddot{I}^{IJ} = R^{iI} R^{jJ} A^{ij} \tag{64}$$

FIG. 10. Discrete time series of the pulsar period and time segment associated with the pulse width solved from $\hat{m} \cdot \hat{n} = \cos \rho$ with $\hat{m} \cdot \hat{n}$ from Fig. 8 and $\rho = 0.6$ rad. The left plots are for the solution tp-I where the lines are generated by Eqs. (51) and (56). The right plots are for the solution tp-II where Eqs. (51) and (56) fail to approximate the discrete points and the lines are spline interpolations of the discrete points.

with the help of the derivative of Eq. (62). The body-frame tensor A^{ij} is lengthy in general but much simplified when the body frame diagonalizes the moment of inertia tensor, which is the case in our setup. The components then read

$$A^{xx} = 2(\Delta_2(\Omega^y)^2 - \Delta_3(\Omega^z)^2),$$

$$A^{yy} = 2(\Delta_3(\Omega^z)^2 - \Delta_1(\Omega^x)^2),$$

$$A^{zz} = 2(\Delta_1(\Omega^x)^2 - \Delta_2(\Omega^y)^2),$$

$$A^{xy} = \left(\frac{(\Delta_3)^2}{I^{zz}} + \Delta_1 - \Delta_2\right)\Omega^x\Omega^y + \frac{\Delta_3}{I^{zz}}\Gamma^z,$$

$$A^{xz} = \left(\frac{(\Delta_2)^2}{I^{yy}} + \Delta_3 - \Delta_1\right)\Omega^x\Omega^z + \frac{\Delta_2}{I^{yy}}\Gamma^y,$$

$$A^{yz} = \left(\frac{(\Delta_1)^2}{I^{xx}} + \Delta_2 - \Delta_3\right)\Omega^y\Omega^z + \frac{\Delta_1}{I^{xx}}\Gamma^x, \quad (65)$$

where $(\Omega^x, \Omega^y, \Omega^z)$ are the body-frame velocity components given in terms of the Euler angles and their derivatives in Eqs. (22), and the body-frame torque components $(\Gamma^x, \Gamma^y, \Gamma^z)$ can be calculated from the anisotropic potential δU via

$$\Gamma^x = -\frac{\sin\gamma}{\sin\beta}\partial_\alpha\delta U - \cos\gamma\partial_\beta\delta U + \cot\beta\sin\gamma\partial_\gamma\delta U,$$

$$\Gamma^y = -\frac{\cos\gamma}{\sin\beta}\partial_\alpha\delta U + \sin\gamma\partial_\beta\delta U + \cot\beta\cos\gamma\partial_\gamma\delta U,$$

$$\Gamma^z = -\partial_\gamma\delta U. \quad (66)$$

The symbols Δ_1, Δ_2, and Δ_3 follow the definition of Zimmermann [35],

$$\Delta_1 = I^{yy} - I^{zz}, \quad \Delta_2 = I^{zz} - I^{xx}, \quad \Delta_3 = I^{xx} - I^{yy}. \quad (67)$$

It is plain that Eqs. (65) go back to the result of Zimmermann [35] when $\Gamma = 0$.

As we restrict ourselves to spheroids, the tensor A^{ij} is further simplified by $I^{xx} = I^{yy}$ and $\Gamma^z = 0$. In the absence of Lorentz violation, the star precesses freely, and the tensor $\ddot{I}^{IJ}$ has a simple form,

$$\ddot{I}^{IJ} = \frac{1}{2}\Delta_2\dot{\alpha}^2\sin 2\beta$$

$$\times \begin{pmatrix} 2\cos 2\alpha\tan\beta & 2\sin 2\alpha\tan\beta & -\sin\alpha \\ 2\sin 2\alpha\tan\beta & -2\cos 2\alpha\tan\beta & \cos\alpha \\ -\sin\alpha & \cos\alpha & 0 \end{pmatrix}, \quad (68)$$

which tells that h^{IJ} is a spherical wave with exactly two frequency components, namely, $\dot{\alpha}$ and $2\dot{\alpha}$. When Lorentz violation presents and the star is subjected to the twofold-precession motion, the tensor $\ddot{I}^{IJ}$ becomes complicated as $\dot{\beta}$ no longer vanishes. But if we only consider motions given by the perturbation solution, we expect Eq. (68) to be a fair approximation and that the continuous GW still has two frequency components $\dot{\alpha}$ and $2\dot{\alpha}$, with $\dot{\alpha}$ being the Lorentz-violating shifted angular frequency given by the first equation in Eqs. (57).

For an observer with colatitude θ_o and azimuth ϕ_o in the X-Y-Z frame, the basis to decompose the 2 physical degrees of freedom for the continuous GW can be taken as
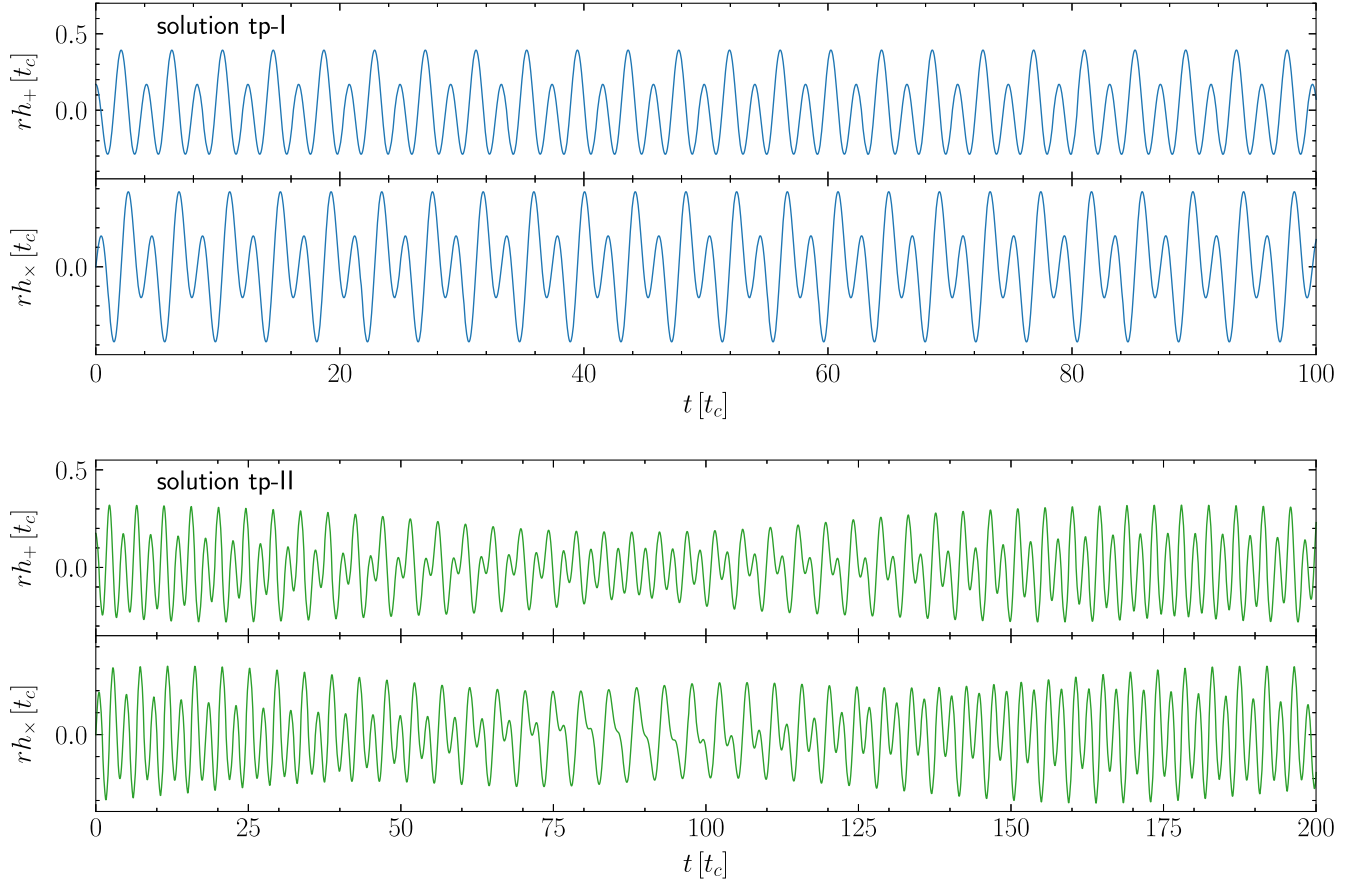
FIG. 11.   Continuous GWs from NSs subjected to the solutions tp-I and tp-II. The angular coordinates of the observer are taken to be $\theta_o = 0.8$ rad and $\phi_o = 0$ in the plots. Time and distance are parametrized using the time unit t_c defined in Eq. (35), which is at the order of 10^{-3} s with our choice of $\epsilon_r = 0.1$ in the numerical solutions and $\rho_{\rm NS} \sim 10^{15}$ g/cm^3 assumed for the density of the NS.

$$e_+ \equiv \hat{\boldsymbol{\theta}}_o \otimes \hat{\boldsymbol{\theta}}_o - \hat{\boldsymbol{\phi}}_o \otimes \hat{\boldsymbol{\phi}}_o, \qquad e_\times \equiv \hat{\boldsymbol{\theta}}_o \otimes \hat{\boldsymbol{\phi}}_o + \hat{\boldsymbol{\phi}}_o \otimes \hat{\boldsymbol{\theta}}_o,$$
$$\tag{69}$$

where

$$\hat{\boldsymbol{\theta}}_o = \cos\theta_o \cos\phi_o \hat{\boldsymbol{e}}_X + \cos\theta_o \sin\phi_o \hat{\boldsymbol{e}}_Y - \sin\theta_o \hat{\boldsymbol{e}}_Z,$$
$$\hat{\boldsymbol{\phi}}_o = -\sin\phi_o \hat{\boldsymbol{e}}_X + \cos\phi_o \hat{\boldsymbol{e}}_Y. \tag{70}$$

Then, the "+" and the "×" components of the continuous GW are

$$h_+ = \frac{1}{2}(\hat{\theta}_o^I \hat{\theta}_o^J - \hat{\phi}_o^I \hat{\phi}_o^J)h^{IJ} = -\frac{1}{r}(\hat{\theta}_o^I \hat{\theta}_o^J - \hat{\phi}_o^I \hat{\phi}_o^J)\ddot{I}^{IJ},$$
$$h_\times = \frac{1}{2}(\hat{\theta}_o^I \hat{\phi}_o^J + \hat{\phi}_o^I \hat{\theta}_o^J)h^{IJ} = -\frac{1}{r}(\hat{\theta}_o^I \hat{\phi}_o^J + \hat{\phi}_o^I \hat{\theta}_o^J)\ddot{I}^{IJ}, \quad (71)$$

where $\hat{\theta}_o^I$ and $\hat{\phi}_o^I$ are the components of $\hat{\boldsymbol{\theta}}_o$ and $\hat{\boldsymbol{\phi}}_o$ in the X-Y-Z frame as shown in Eqs. (70).

When continuous GWs from NSs are detected, Eqs. (71) can be used as template waveforms to match observational data. Similar to the analysis of the pulsar signal in Sec. III B,

to extract the coefficients for Lorentz violation $\bar{s}^{XX}, \bar{s}^{YY}, \bar{s}^{ZZ}$ and the NS parameters $\epsilon, \Omega^z, \theta_o, r$ from observational data, elaborate numerical calculations are required. Using the two numerical solutions in Figs. 2 and 3 to calculate $\ddot{I}^{IJ}$, we plot the corresponding waveforms in Fig. 11 and their Fourier transformations in Fig. 12. Tiny high frequency components in the spectra are found. They are featured in the subplots of Fig. 12 and turn out to be exactly 3 times the fundamental frequencies, which are represented by the peaks near $1.438\, t_c^{-1}$ and can be regarded as the average values of $\dot{\alpha}$ for the twofold-precession motions. Frequencies higher than the third harmonic exist, but their amplitudes are even much smaller. We point out that unlike the pulsar signal of solution tp-II, there is no low frequency at the order of the coefficients for Lorentz violation in the continuous GW spectra. However, the advantage of a continuous GW signal is that both solutions tp-I and tp-II exhibit the third harmonic characterizing the deviation of the waveform from that of a free-precessing NS, though in the case of solution tp-I, the amplitude of the third harmonic is further suppressed. This Lorentz-violating feature is worth looking for and may reveal new physics beyond the current understanding.
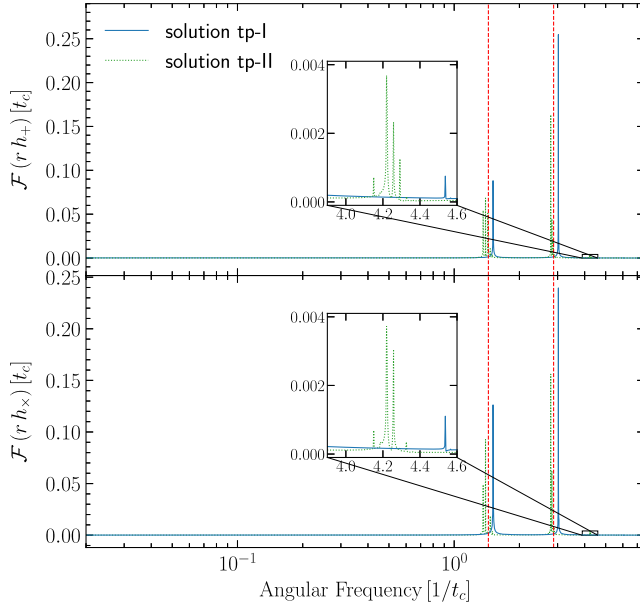
FIG. 12. Fourier transformations for the continuous GWs shown in Fig. 11. The dashed red vertical lines mark $\dot{\alpha} \approx 1.438$ and $2\dot{\alpha} \approx 2.876$, which are the angular frequencies of the continuous GWs from a free-precessing NS with $I^{zz}/I^{xx} = 1.1$, $\Omega^z = 1$, and $\beta = 0.7$. As we have taken $\epsilon_r = 0.1$, the frequency unit is $1/t_c \sim 1000$ rad/s if the density of the NS is $\rho_{NS} \sim 10^{15}$ g/cm^3.

IV. CONCLUSION

Lorentz violation modifies the Newtonian potential by an anisotropic correction, generating a torque on spheroidal stars that forces the otherwise conserved angular momentum of the star to precess around a preferred direction defined by the coefficients for Lorentz violation. To solve the motion rigorously, we first calculate the anisotropic gravitational self-energy of the star caused by Lorentz violation in the minimal gravitational SME in Sec. II A. The result is proved to be equivalent to that of Nordtvedt [17] when the star is treated as a stationary spinning fluid star in equilibrium so the tensor virial relation holds. Discrepancy occurs when the star possesses a rigid deformation which invalidates the tensor virial relation. Besides stationary spin, free precession is also a solution of motion for such stars in the absence of torques.

Then in Sec. II B, the forced precession caused by the Lorentz-violating torque on stationary spinning stars and on free-precessing stars is explicitly calculated using the perturbation method to solve the rotational equations of motion. Interestingly, we find that the direction of the forced precession on stationary spinning stars is opposite to the direction of the forced precession on free-precessing stars as shown in Eq. (32). Numerical solutions are explored to check the validity of the perturbation approach. Initial values for which the perturbation approach fails are identified. The study of the solutions is finished by clarifying that the preferred directions around which the forced precession happens are exactly the eigenvectors of the matrix $\bar{s}^{ij}$. An

interesting result is that when the matrix $\bar{s}^{ij}$ acquires three different eigenvalues, the forced precession is unstable if it is around the eigenvector corresponding to the middle eigenvalue. This is similar to the well-known Dzhanibekov effect (or the tennis racket theorem).

After the solutions of motion are studied thoroughly, we apply them to explore the observational consequences for NSs in Sec. III. Section III A treats the two solitary pulsars in Ref. [29] as stationary spinning spheroids at zeroth order, and sets bounds on the coefficients for Lorentz violation by attributing any possible tiny alteration of the NSs' orientations hidden in observational uncertainties to the forced precession due to Lorentz violation. With the connection between the SME coefficients $\bar{s}^{ij}$ and the PPN coefficient α_2 shown in Eq. (5), the constraints obtained here are consistent with the ones for the α_2 coefficient in Ref. [29]. However, our "maximal-reach" constraints obtained from the two solitary pulsars are 3 to 5 orders of magnitude better than those in Ref. [14]. The same two solitary pulsars are used there but together with another 11 binary pulsars for a global analysis. Notice that here we use a different coordinate frame from that of Ref. [14], so a plain comparison is only heuristic. Nevertheless, this suggests that the orbital motions of the binary pulsars are less sensitive to Lorentz violation than the rotational motions of the solitary pulsars. Therefore, we urge observers to analyze the stability of pulsar spins—possibly via the pulse profile stability as it was done by Shao et al. [29]—with more suitable systems and to put tighter bounds on the coefficients for Lorentz violation.

In Secs. III B and III C, pulsar signals and continuous GWs from Lorentz-violating-affected free-precessing NSs are investigated. When the angular momentum of the star is close to the preferred direction around which the forced precession happens, the spectra of the signals are very much like those from a free-precessing NS. The forced precession does shift frequencies in the spectra, but the contribution from it is practically unable to be decoupled from the free-precessing frequency components. When the angular momentum of the star makes a relatively large angle to the preferred direction around which the forced precession happens, decisive characteristics that are worth searching for show up in the spectra. For pulsar signals, the signature is an extremely low frequency component as shown in the lower plot of Fig. 9. The observables, namely, the pulsar period and the pulse width, are not only modulated by the average rate of the Euler angle γ, but also modulated by this frequency (right plots in Fig. 10). The polarization characteristics of pulsar pulses are interesting to investigate in future studies, and they could provide more information on the rotation of the NS and its radiation properties. For GWs, the signature is represented by the third harmonic shown in the subplots of Fig. 12. Free-precessing spheroidal NSs emit continuous GWs only at the first and the second harmonics of the rate of the Euler angle α. But once affected by Lorentz violation, the continuous GW emitted by the star is no longer a simple sum

of sinusoidal functions. The waveform generally involves all harmonics of the average rate of the Euler angle α, with the amplitudes decreasing rapidly after the first two.

The characteristic frequencies in the spectra of the signals are qualitative support for Lorentz violation if observed. To extract quantitative values of the coefficients for Lorentz violation, as well as the physical parameters of the NS, numerical calculations are necessary to fit the observational data. Tentative candidates of free-precessing NSs are proposed in pulsar observations [31,36], while searches for continuous GWs have not yet confidently identified any positive detections [37–42]. Our study supplies the necessary templates for potential new tests of Lorentz violation that take advantage of the two state-of-the-art observation channels in the era of multimessenger astronomy. Once free-precessing NSs are unambiguously identified, the new tests using their modulated pulsar signals and continuous GWs are bound to enrich our fundamental knowledge on Lorentz symmetry of our spacetime.

ACKNOWLEDGMENTS

APPENDIX: THE CONSTANT C FOR UNIFORM SPHEROIDS

Using the results on Maclaurin spheroids summarized in Refs. [20,21], we can explicitly write down the constant C in terms of the eccentricity defined as

$$e \equiv \sqrt{1 - \left(\frac{a_3}{a_1}\right)^2} \tag{A1}$$

for a spheroid (10) with uniform density. We start with the Newtonian potential (16) inside an ellipsoid of uniform density,

$$\Phi = -\pi\rho(A_0 - A_1 x^2 - A_2 y^2 - A_3 z^2). \tag{A2}$$

The constants A_0, A_1, A_2, and A_3 happen to have closed-form results for spheroids,

$$A_0 = 2a_1^2 \sqrt{1-e^2} \frac{\arcsin e}{e} = 2a_1^2 \left(1 - \frac{1}{3}e^2 + O(e^4)\right),$$

$$A_1 = A_2 = \frac{\sqrt{1-e^2}}{e^2}\left(\frac{\arcsin e}{e} - \sqrt{1-e^2}\right) = \frac{2}{3}\left(1 - \frac{1}{5}e^2 + O(e^2)\right),$$

$$A_3 = \frac{2}{e^2}\left(1 - \sqrt{1-e^2}\frac{\arcsin e}{e}\right) = \frac{2}{3}\left(1 + \frac{2}{5}e^2 + O(e^2)\right). \tag{A3}$$

It then follows that the constant C is

$$C = \frac{1}{2}(U^{xx} - U^{zz}) = \frac{4\pi^2}{15}\rho^2 a_1^2 a_3 (a_1^2 A_1 - a_3^2 A_3)$$

$$= \frac{16\pi^2}{225}\rho^2 a_1^4 a_3 (e^2 + O(e^4)). \tag{A4}$$

We point out that the equilibrium condition

$$\frac{p}{\rho} = -\Phi + \frac{1}{2}|\mathbf{\Omega}|^2(x^2 + y^2) + \text{const} \tag{A5}$$

on the surface where $p = 0$ implies

$$|\mathbf{\Omega}|^2 = 2\pi\rho\left(A_1 - \frac{a_3^2}{a_1^2}A_3\right). \tag{A6}$$

As the angular velocity $\mathbf{\Omega}$ is along the z axis, we directly see

$$T_{\text{rot}} = \frac{1}{2}I^{zz}|\mathbf{\Omega}|^2 = 2C, \tag{A7}$$

where $I^{zz} = 8\pi/15\rho a_1^4 a_3$ has been used. It is also worth pointing out that both the eccentricity defined in Eq. (A1) and the oblateness defined in Eq. (19) characterize the deviation of a spheroid from a sphere. For a uniform spheroid, they are simply related via

$$\epsilon = \frac{e^2}{2 - e^2}. \tag{A8}$$

[1] V. A. Kostelecký and S. Samuel, Phys. Rev. D **39,** 683 (1989).
[2] V. A. Kostelecký and S. Samuel, Phys. Rev. Lett. **63,** 224 (1989).
[3] V. A. Kostelecký and R. Potting, Nucl. Phys. **B359,** 545 (1991).
[4] C. M. Will and K. Nordtvedt, Jr., Astrophys. J. **177,** 757 (1972).
[5] C. M. Will, *Theory and Experiment in Gravitational Physics* (Cambridge University Press, Cambridge, England, 2018).
[6] V. A. Kostelecký and N. Russell, Rev. Mod. Phys. **83,** 11 (2011).
[7] L. Shao and N. Wex, Sci. China Phys. Mech. Astron. **59,** 699501 (2016).
[8] D. Colladay and V. A. Kostelecký, Phys. Rev. D **55,** 6760 (1997).
[9] D. Colladay and V. A. Kostelecký, Phys. Rev. D **58,** 116002 (1998).
[10] V. A. Kostelecký, Phys. Rev. D **69,** 105009 (2004).
[11] Q. G. Bailey and V. A. Kostelecký, Phys. Rev. D **74,** 045001 (2006).
[12] R. Bluhm and V. A. Kostelecký, Phys. Rev. D **71,** 065008 (2005).
[13] Q. G. Bailey, V. A. Kostelecký, and R. Xu, Phys. Rev. D **91,** 022006 (2015).
[14] L. Shao, Phys. Rev. Lett. **112,** 111103 (2014).
[15] Y. Gao, L. Shao, R. Xu, L. Sun, C. Liu, and R.-X. Xu, Mon. Not. R. Astron. Soc. **498,** 1826 (2020).
[16] C. M. Will, Living Rev. Relativity **17,** 4 (2014).
[17] K. Nordtvedt, Astrophys. J. **320,** 871 (1987).
[18] L. D. Landau and E. M. Lifshitz, *Mechanics* (Butterworth-Heinemann, Oxford, 1960), https://doi.org/10.1016/C2009-0-25569-3.
[19] R. Xu and Y. Gao, and L. Shao, Galaxies **9,** 12 (2021).
[20] E. Poisson and C. M. Will, *Gravity: Newtonian, Post-Newtonian, Relativistic* (Cambridge University Press, Cambridge, England, 2014).
[21] S. Chandrasekhar and N. R. Lebovitz, Astrophys. J. **136,** 1037 (1962).
[22] D. I. Jones and N. Andersson, Mon. Not. R. Astron. Soc. **324,** 811 (2001).
[23] M. Zimmermann and E. Szedenits, Phys. Rev. D **20,** 351 (1979).
[24] Y. Gao and L. Shao, Astron. Nachr. **342,** 364 (2021).
[25] B. Altschul, Phys. Rev. D **75,** 023001 (2007).
[26] R. Xu, J. Zhao, and L. Shao, Phys. Lett. B **803,** 135283 (2020).
[27] V. A. Kostelecký and M. Mewes, Phys. Rev. D **66,** 056005 (2002).
[28] L. Poinsot, *Theórie Nouvelle de la Rotation des Corps* (Bachelier, Paris, 1851).
[29] L. Shao, R. N. Caballero, M. Kramer, N. Wex, D. J. Champion, and A. Jessner, Classical Quantum Gravity **30,** 165019 (2013).
[30] L. Shao, in *Proceedings of the 8th Meeting on CPT and Lorentz Symmetry* (2020), pp. 170–173 [arXiv:1905.08405].
[31] I. Stairs, A. Lyne, and S. Shemar, Nature (London) **406,** 484 (2000).
[32] D. R. Lorimer and M. Kramer, *Handbook of Pulsar Astronomy* (Cambridge University Press, Cambridge, England, 2005).
[33] J. D. Tasson, in *Proceedings of the 8th Meeting on CPT and Lorentz Symmetry* (2020), pp. 13–16 [arXiv:1907.08106].
[34] J. Gil, P. Gronkowski, and W. Rudnicki, Astron. Astrophys. **132,** 312 (1984), https://ui.adsabs.harvard.edu./abs/1984A%26A...132..312G/abstract.
[35] M. Zimmermann, Phys. Rev. D **21,** 891 (1980).
[36] T. Shabanova, A. Lyne, and J. Urama, Astrophys. J. **552,** 321 (2001).
[37] B. Abbott *et al.* (LIGO Scientific and Virgo Collaborations), Phys. Rev. D **100,** 024004 (2019).
[38] P. B. Covas and A. M. Sintes, Phys. Rev. Lett. **124,** 191102 (2020).
[39] V. Dergachev and M. A. Papa, Phys. Rev. Lett. **125,** 171101 (2020).
[40] M. A. Papa, J. Ming, E. V. Gotthelf, B. Allen, R. Prix, V. Dergachev, H.-B. Eggenstein, A. Singh, and S. J. Zhu, Astrophys. J. **897,** 22 (2020).
[41] B. Steltner, M. Papa, H.-B. Eggenstein, B. Allen, V. Dergachev, R. Prix, B. Machenschalk, S. Walsh, S. Zhu, and S. Kwang, Astrophys. J. **909,** 79 (2021).
[42] Y. Zhang, M. A. Papa, B. Krishnan, and A. L. Watts, Astrophys. J. Lett. **906,** L14 (2021).